Univerzita Karlova v Praze

Matematicko-fyzikální fakulta

BAKALÁŘSKÁ PRÁCE

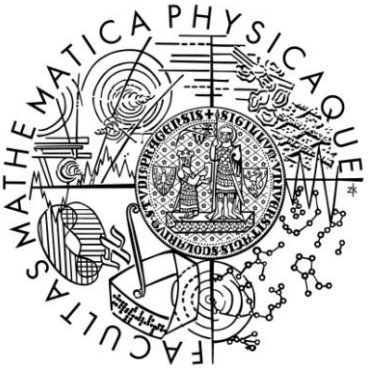

Attila Bartha

Studium nových silně korelovaných elektronových sloučenin $RE_nT\mathrm{In}_{3n+2}$

Katedra fyziky kondenzovaných látek

Vedoucí bakalářské práce: RNDr. Marie Kratochvílová

Studijní program: Fyzika

Studijní obor: Obecná fyzika

Praha 2013

Charles University in Prague

Faculty of Mathematics and Physics

BACHELOR THESIS

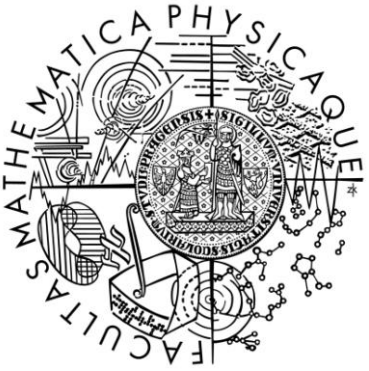

Attila Bartha

The study of new strongly correlated electron systems $RE_nT\text{In}_{3n+2}$

Department of Condensed Matter Physics

Supervisor of the bachelor thesis: RNDr. Marie Kratochvílová

Study programme: Physics

Specialization: General Physics

Prague 2013

I would like to express my honest gratitude to my supervisor RNDr. Marie Kratochvílová, for her patience, helpful advices and time she devoted to me. Also, I would like to thank doc. RNDr. Martin Diviš, CSc. for the theoretical calculations of electronic band structure of RE_2CoIn_8. Finally, I would like to express my thanks to my family that always supported me during my studies.

I declare that I carried out this bachelor thesis independently, and only with the cited sources, literature and other professional sources.

I understand that my work relates to the rights and obligations under the Act No. 121/2000 Coll., the Copyright Act, as amended, in particular the fact that the Charles University in Prague has the right to conclude a license agreement on the use of this work as a school work pursuant to Section 60 paragraph 1 of the Copyright Act.

In Prague

Název práce: Studium nových silně korelovaných elektronových sloučenin $RE_nT\mathrm{In}_{3n+2}$

Autor: Attila Bartha

Katedra / Ústav: Katedra fyziky kondenzovaných látek (KFKL)

Vedoucí bakalářské práce: RNDr. Marie Kratochvílová, Katedra fyziky kondenzovaných látek (KFKL)

Abstrakt: Zabývali jsme se studiem systému sloučenin $RE_2\mathrm{CoIn}_8$ (*RE* = Pr, Nd, Dy) a $\mathrm{Ce}_nT\mathrm{In}_{3n+2}$ (*T* = Pd, Pt; *n* = 2, 3). Všechny materiály byly připraveny poprvé ve formě monokrystalů metodou růstu z vlastního fluxu. Rentgenová difrakce potvrdila, že jak sloučeniny $RE_2\mathrm{CoIn}_8$, tak i nová fáze $\mathrm{Ce}_2\mathrm{PtIn}_8$ krystalizují v tetragonální soustavě typu $\mathrm{Ho}_2\mathrm{CoGa}_8$. $\mathrm{Ce}_3\mathrm{PtIn}_{11}$ je taktéž novou sloučeninou, která přejímá krystalovou soustavu po novém strukturním typu $\mathrm{Ce}_3\mathrm{PdIn}_{11}$. Magnetická měření odhalila nízkou anizotropii a osu *c* jako snadnou osu magnetizace pro všechny $RE_2\mathrm{CoIn}_8$. $\mathrm{Pr}_2\mathrm{CoIn}_8$ je paramagnetická, zatímco $\mathrm{Nd}_2\mathrm{CoIn}_8$ a $\mathrm{Dy}_2\mathrm{CoIn}_8$ se uspořádávají antiferomagneticky. Na základě měření magnetizace a měrného tepla byl sestaven komplexní *H-T* fázový diagram sloučeniny $\mathrm{Dy}_2\mathrm{CoIn}_8$ s různými typy magnetického uspořádání. Měrné teplo vícefázového vzorku Ce-Pd-In vykazuje supravodivý přechod při T_c = 0.69 K pocházející od $\mathrm{Ce}_2\mathrm{PdIn}_8$ a další, tentokrát magnetický přechod při teplotě ~ 1.7 K příslušející sloučenině $\mathrm{Ce}_3\mathrm{PdIn}_{11}$. V měrném teple sloučenin $\mathrm{Ce}_3\mathrm{PdIn}_{11}$ a $\mathrm{Ce}_3\mathrm{PtIn}_{11}$ pozorujeme dva, pravděpodobně magnetické přechody při teplotách T_1 = 1.6 K a T_2 = 1.45 K, respektive T_1 = 2.1 K a T_2 = 2.0 K. Oba materiály jsou těžkofermionovými sloučeninami vzhledem k jejich Sommerfeldovým koeficientům γ = 290 $\mathrm{mJ.mol^{-1}Ce\ K^{-2}}$, respektive γ = 300 $\mathrm{mJ.mol^{-1}Ce\ K^{-2}}$.

Klíčová slova: $RE_nT\mathrm{In}_{3n+2}$, antiferomagnetismus, těžkofermionové chování, měrné teplo

Title: The study of new strongly correlated electron systems $RE_nT\mathrm{In}_{3n+2}$

Author: Attila Bartha

Department / Institute: Department of Condensed Matter Physics

Supervisor of the bachelor thesis: RNDr. Marie Kratochvílová, Department of Condensed Matter Physics

Abstract: We have studied two different systems; $RE_2\mathrm{CoIn}_8$ (*RE* = Pr, Nd, Dy) and $\mathrm{Ce}_nT\mathrm{In}_{3n+2}$ (*T* = Pd, Pt; *n* = 2, 3). All compounds were prepared for the first time in the single crystalline form using the self-flux method. *X*-ray diffraction confirmed the tetragonal $\mathrm{Ho}_2\mathrm{CoGa}_8$ structure type for the $RE_2\mathrm{CoIn}_8$ compounds and for the new phase $\mathrm{Ce}_2T\mathrm{In}_8$. The novel phase $\mathrm{Ce}_3\mathrm{PtIn}_{11}$ adopts the structure of the $\mathrm{Ce}_3\mathrm{PdIn}_{11}$ compound, which represents a new structure type. Magnetic measurements revealed low anisotropy and the *c*-axis as the easy axis for all $RE_2\mathrm{CoIn}_8$ compounds. $\mathrm{Pr}_2\mathrm{CoIn}_8$ is a paramagnet, while $\mathrm{Nd}_2\mathrm{CoIn}_8$ and $\mathrm{Dy}_2\mathrm{CoIn}_8$ order antiferromagnetically. Magnetization and specific heat measurements of $\mathrm{Dy}_2\mathrm{CoIn}_8$ revealed complex magnetic field-temperature phase diagram with various types of magnetic ordering. Specific heat measurements on multiphase Ce-Pd-In system revealed superconducting transition at T_c = 0.69 K arising from $\mathrm{Ce}_2\mathrm{PdIn}_8$ and another magnetic transition from $\mathrm{Ce}_3\mathrm{PdIn}_{11}$ at ~ 1.7 K. $\mathrm{Ce}_3\mathrm{PdIn}_{11}$ and $\mathrm{Ce}_3\mathrm{PtIn}_{11}$ compounds reveal two, probably magnetic transitions at T_1 = 1.6 K, T_2 = 1.45 K and T_1 = 2.1 K and T_2 = 2.0 K, respectively. Specific heat data qualifies both materials as heavy fermion compounds with γ = 290 $\mathrm{mJ.mol^{-1}Ce\ K^{-2}}$ and γ = 300 $\mathrm{mJ.mol^{-1}Ce\ K^{-2}}$ respectively.

Keywords: $RE_nT\mathrm{In}_{3n+2}$, antiferromagnetism, heavy-fermion behaviour, specific heat

Contents

Introduction

Intermetallic compounds containing *f*-electron elements display a plethora of magnetic and superconducting ground states. The work "The study of new strongly correlated electron systems $RE_nT\mathrm{In}_{3n+2}$" is devoted to the synthesis and the investigation of physical properties of the new $RE_nT\mathrm{In}_{3n+2}$ (*RE* = rare earth, *T* = transition metal, *n* = 2, 3) compounds in the single crystalline form. These compounds have become the subject of intensive studies more than one decade ago because they provide a considerable opportunity to study interesting phenomena including heavy fermion behaviour (HF), various types of magnetic ordering or anisotropic properties due to dimensionality. In these systems, the quantum critical point (QCP) can be tuned by applying pressure, substitutional doping [52], and also by varying the dimensionality going from more 2D-like $RET\mathrm{In}_5$ to 3D-like $RE_2T\mathrm{In}_8$. We focus intensively on the refinement of the synthesis as these materials are prepared solely by the solution growth method. Although this technique suffers from several disadvantages compared to other methods, its versatility provides a unique possibility to prepare new ternary systems from the $RE_nT\mathrm{In}_{3n+2}$ family of compounds.

Motivation

The work is based on two main topics:

In the first part we have studied the synthesis and physical properties of the $RE_2\mathrm{CoIn}_8$ (*RE* = Pr, Nd, Dy) compounds. These magnetic materials are important for understanding the evolution of the *f*-electron magnetism in their isostructural cerium analogs. Unlike the majority of the $RE_nT\mathrm{In}_{3n+2}$ compounds, $RE_2\mathrm{CoIn}_8$ have not been studied in the single crystalline form yet. The theoretical predictions [62] motivated us to find the optimal growth conditions to be able to investigate the anisotropic properties of $\mathrm{Pr}_2\mathrm{CoIn}_8$, $\mathrm{Nd}_2\mathrm{CoIn}_8$ and $\mathrm{Dy}_2\mathrm{CoIn}_8$ single crystals.

In the second section, we have focused on the investigation of structural and physical properties of the new $\mathrm{Ce}_nT\mathrm{In}_{3n+2}$ (*T* = Pd, Pt; *n* = 2, 3) materials. Since the compounds from the $\mathrm{Ce}_nT_m\mathrm{In}_{3n+2m}$ family reveal many unusual properties such as unconventional superconductivity [18, 19], they represent a contrast to purely non-Kondo properties of the $RE_2\mathrm{CoIn}_8$ compounds studied in the other part of the thesis. The ambiguous growth conditions of the $\mathrm{Ce}_2\mathrm{PdIn}_8$ phase [63] prevent us from

preparation of the single crystals in dimensions sufficient for many measurement techniques. This experimental limitation represents our crucial motivation regarding the single crystal growth. Moreover, the recent discoveries of the new structure types Ce_3PdIn_{11} and $Ce_5Pd_2In_{19}$ [40] within the $RE_nT_mIn_{3n+2m}$ family broadened our area of interest, as they represent a great possibility of testing the parameter "dimensionality". Tuning of the ground state of these new compounds can contribute to clarification of the extended Doniach phase diagram [99].

1. Physics of *RE* compounds

1.1. Strongly correlated electron systems

Let us focus our interest on the magnetism of *4f* electron systems. Generally, valence *s* and *p* electrons are considered to be delocalized, while 4*f* electrons are localized and 5*f* and 3*d*/4*d* electrons are intermediate, depending on their particular internuclear distances [1, 20]. Localized 4*f* electrons lie very close to the nucleus, with negligible overlap of their 4*f*-wave functions [1]. They do not participate in chemical bonds preserving their atomic character. When a magnetic rare earth ion is placed in a solid, various interactions [4] have to be taken into account as shown later in the text. On the other hand, for delocalized (itinerant) electrons a new quantum number is needed to describe the quantum state and discrete energy levels are to be replaced by quasi-continuous energy levels. Electron states are given by plane waves (Bloch states) periodically extending over the whole crystal. Magnetic moments appear to be smeared out (delocalized) over the whole crystal [28].

Systems with a strong hybridization between the inner *d* or *f* electrons and the conduction electrons are called *strongly correlated electron systems* (SCES) [5]. The SCES physics has been the subject of intensive experimental and theoretical studies for almost a half of the century. While conduction electrons (in simple metals) are uncorrelated and exhibit free-electron-like behaviour, SCES reveal phenomena which cannot be described by the behaviour of individual particles and correlations have to be included. The main topic concerns materials, which exhibit HF behaviour [11]. HF materials are inherently close to Quantum critical point (QCP) and hence suitable to investigate quantum criticality. Critical behaviour is accompanied with emergence of unconventional superconductivity, coexistence of magnetic ordering and superconductivity, non-Fermi liquid behaviour and other unusual phenomena [47, 48, 49].

An atom (ion) has a nonzero magnetic moment when a *d*- or *f*- shell is partially filled so the individual electronic moments do not cancel each other completely. The ground state of such atom is given by *Hund's rules* and can be summarized using *term-symbols*: $^{2S+1}L_J$, where **S** and **L** is the total spin and orbital momentum, respectively, and **J** is the total angular momentum. In case of *RE* the ground state obtained by Hund's rules is in good agreement with experimental data because of the

localized character of the *4f* electrons [1]. Difference between values of magnetic moments predicted by Hund's rules and experimental data is caused by the crystal field (CF) effects. CF interaction can be described using full free-ion Hamiltonian [2, 3]:

$$\hat{H} = \hat{H}_0 + \hat{H}_{res} + \hat{H}_{SO} + \hat{H}_{CF} \qquad (1)$$

Hamiltonian $\hat{H}_0$ represents the kinetic energy of N electrons in the atom, at positions $\vec{r}_i$ with electrostatic potential of nuclei and effective potential $V_{ef}(\vec{r}_i)$:

$$\hat{H}_0 = \sum_{i=1}^{N}\left(\frac{\hat{p}_i^2}{2m_e} - \frac{Ze'^2}{r_i} + V_{ef}(\vec{r}_i)\right) \qquad (2)$$

where $\hat{\vec{p}}_i$ is the linear momentum of the i^{th} electron, m_e is the mass of the electron and Z is the atomic number. The effective potential represents Coulomb and exchange interaction from Hartree-Fock approximation. Residual interaction $\hat{H}_{res}$ is a perturbation which takes the form:

$$\hat{H}_{res} = \sum_{i\neq j}\frac{e'^2}{|\vec{r}_i - \vec{r}_j|} - \sum_{i=1}^{N} V_{ef}(\vec{r}_i) \qquad (3)$$

Spin-orbit interaction $\hat{H}_{SO}$ is a relativistic effect, describing the coupling of **S** and **L**. They are no longer good quantum numbers and together, they define total angular momentum **J = L + S**. One can write

$$H = \lambda\,(\mathbf{L.S}) \qquad (4)$$

within *LS* coupling scheme, where λ is a constant factor for a given *LS* state.

Crystal field perturbation $\hat{H}_{CF}$ represents the local environment due to crystal symmetry [3]:

$$\hat{H}_{CF} = \sum_{L,M} B_L^M \hat{O}_L^M \qquad (5)$$

where B_L^M represents symmetry dependent CF parameters and $\hat{O}_L^M$ CF operators summed over orbital and magnetic quantum numbers. $\hat{H}_{CF}$ and $\hat{H}_{SO}$ represent a main source of magnetic anisotropy [4].

1.2. Magnetic moments

The basic objects in magnetism are magnetic moments.

In the classical approach a magnetic moment $\boldsymbol{\mu}$ is equivalent to an electric charge orbiting in a circle, so called *current loop*. Definition of the magnetic moment is

$$\mathbf{d}\boldsymbol{\mu} = I\mathbf{dS} \tag{6}$$

where I is an electric current in the loop and $|\mathbf{dS}|$ is the area of the loop. The direction of the vector $\mathbf{d}\boldsymbol{\mu}$ is always normal to the current loop [1].

Quantum mechanics ascribes the origin of the free magnetic moment to three principal sources: the orbital moment, the spin moment and the interaction of the orbital moment with an external field [8]. Hamiltonian of a free atom (ion) in an applied magnetic field can be written as [6]:

$$\hat{H} = \hat{H}^{(0)} + \frac{eB}{2m_e}\left(\hat{L} + 2\hat{S}\right) + \frac{e^2B^2}{8m_e}\sum_{i=1}^{N}\left(x_i^2 + y_i^2\right) \tag{7}$$

$\hat{H}^{(0)}$ is a Hamiltonian of a free atom:

$$\hat{H}^{(0)} = \sum_{i=1}^{N}\left(\frac{\hat{p}_i^2}{2m_e} - \frac{Ze'^2}{r_i}\right) + \sum_{i<j}\frac{e'^2}{r_{ij}} \tag{8}$$

where $r_{ij} = \left|\vec{r}_i - \vec{r}_j\right|$ is the distance between the i^{th} and j^{th} electron.

Magnetization

Magnetization $\boldsymbol{M}$ is defined as the magnetic moment per unit volume; it is linearly proportional to the intensity of magnetic field $\boldsymbol{H}$ and together they define the magnetic susceptibility χ:

$$\boldsymbol{M} = \chi\boldsymbol{H} \tag{9}$$

Magnetic susceptibility χ is a dimensionless quantity which represents the magnetic moment induced by magnetic field $\boldsymbol{H}$ per unit volume. In magnetic materials the general relation between magnetic induction $\boldsymbol{B}$ and magnetic field intensity $\boldsymbol{H}$ can be written as:

$$\boldsymbol{B} = \mu_0(\boldsymbol{H} + \boldsymbol{M}) \tag{10}$$

where μ_0 is the permeability of the free space. In linear materials we can express the relationship between $\boldsymbol{B}$ and $\boldsymbol{H}$ using the relative permeability of material μ_r:

$$\boldsymbol{B} = \mu_0(1+\chi)\boldsymbol{H} = \mu_0\mu_r\boldsymbol{H} \qquad (11)$$

Diamagnetism

Diamagnetism refers to substances with negative magnetic susceptibility. From a classical point of view it can be interpreted using Lenz's law; applied magnetic field induces magnetic moments which oppose the field that created it [29]. A quantum mechanical aspect of diamagnetism can be represented as the third term in Eq. 7. Assuming the first order perturbation theory and spherically symmetric atom [1] we obtain the relation for diamagnetic susceptibility:

$$\chi_{dia} = -\frac{\mu_0 ZNe^2}{6m_e}\left\langle r^2 \right\rangle \qquad (12)$$

where N is the number of atoms per unit volume and $\left\langle r^2 \right\rangle$ is the root mean square atomic radius. Diamagnetism is always present in an external field; however it is often covered by the positive paramagnetic susceptibility. Examples of diamagnetic materials are: noble gases, carbon, tin, zinc, gold, etc.

Superconducting materials reveal ideal diamagnetism due to Meissner - Ochsenfeld effect, with susceptibility $\chi = -1$ [3].

Paramagnetism (PM)

On the other hand, the paramagnetic materials reveal positive magnetic susceptibility which is the consequence of partially filled electron shells. Magnetic moments in the atom are randomly oriented until the external field $\boldsymbol{H}$ is applied and makes these moments align into the direction of the field; therefore the magnetization $\boldsymbol{M}$ is enhanced.

Due to its small influence on the total magnetic moment, we often neglect diamagnetism. Therefore the magnetic moment of an atom is given according to (7) mainly by the paramagnetic part:

$$\boldsymbol{\mu} = \frac{\mu_B}{\hbar}(\boldsymbol{L}+2\boldsymbol{S}) \qquad (13)$$

The parameter $\mu_B = \frac{e\hbar}{2m_e}$, called *Bohr's magneton*, is a convenient unit for describing of the atomic magnetic moment. Relation (13) can be written in an alternative form using the *Landé factor* g_J and total angular momentum $\boldsymbol{J}$: $\boldsymbol{\mu} = -\mu_B g_J \boldsymbol{J}$.

Consequently, the effective magnetic moment is given:

$$\mu_{eff} = \mu_B g_J \sqrt{J(J+1)} \qquad (14)$$

The paramagnetic susceptibility does not depend on magnetic field and it is inversely proportional to temperature T which can be expressed by so called *Curie* constant [11]:

$$C = \frac{n\mu_0 \mu_{eff}^2}{3k_B} \qquad (15)$$

where *n* is the number of spins per unit volume and k_B is the Boltzmann's constant. For paramagnetic susceptibility we obtain a formula called the *Curie-law*:

$$\chi_{para} = \frac{C}{T} \qquad (16)$$

Van Vleck paramagnetism

Van Vleck contribution to the paramagnetic susceptibility often occurs in crystals containing non-Kramer's rare earth ions. In the case of *RE* possessing an even number of 4*f* electrons the lowest electronic ground state is expected to be either singlet or non-magnetic doublet [4]. The low temperature behaviour of the susceptibility is strongly influenced by the CF and another temperature independent contribution emerges.

Exchange interactions

Exchange interactions are crucial for the emergence of long range magnetic ordering. They are electrostatic interactions between electrons arising from the antisymmetric origin of the overall wave function [1]. In the Heisenberg model, the spin-dependent Hamiltonian describing the energy of these interactions is given by:

$$\hat{H} = -\sum_{ij} J_{ij}\, \boldsymbol{S}_i.\boldsymbol{S}_j \qquad (17)$$

where J_{ij} is the exchange integral between the i^{th} and j^{th} electron in the system, $\boldsymbol{S}_i$ and $\boldsymbol{S}_j$ are the spin quantum numbers of i^{th} and j^{th} electron, respectively [4].

There are 3 basic types of exchange interactions [4]:

Direct exchange occurs between neighbouring magnetic atoms, where their wave functions overlap sufficiently. It proceeds without any intermediary; however it is not effective in rear earths due to the strongly localized *4f* electrons. This short range interaction occurs typically in materials containing 3*d*; 4*d*; 5*d* or 5*f* elements.

Indirect exchange (or *superexchange*) describes an interaction between magnetic moments too far apart to be connected by direct exchange. In this case a non-magnetic intermediary material provides the interaction. Superexchange can be found in 3*d*; 4*d*; 5*d* and 4*f*; 5*f* compounds with *p*- and *d*–elements.

RKKY (*Ruderman, Kittel, Kasuya and Yoshida*) *exchange* is a long range interaction between strongly localized *4f* electrons where any direct interaction due to lacking overlap of the wave functions is excluded. It has an oscillatory dependence on the distance between the moments, and can be written as an *r*-dependent exchange interaction

$$J_{RKKY}(r) \propto \frac{\cos(2k_F r)}{r^3} \qquad (18)$$

where we assume a spherical Fermi surface with radius k_F.

Magnetically ordered states

In materials with strongly interacting magnetic moments cooperative phenomena can be observed when the exchange interaction energy exceeds the energy of the thermal movement of magnetic moments. These phenomena lead to a long range periodic magnetic ordering below a critical temperature and as a result, nonzero magnetization is observed in the absence of external field [8]. Basic types of magnetically ordered states are: ferromagnetism and antiferromagnetism.

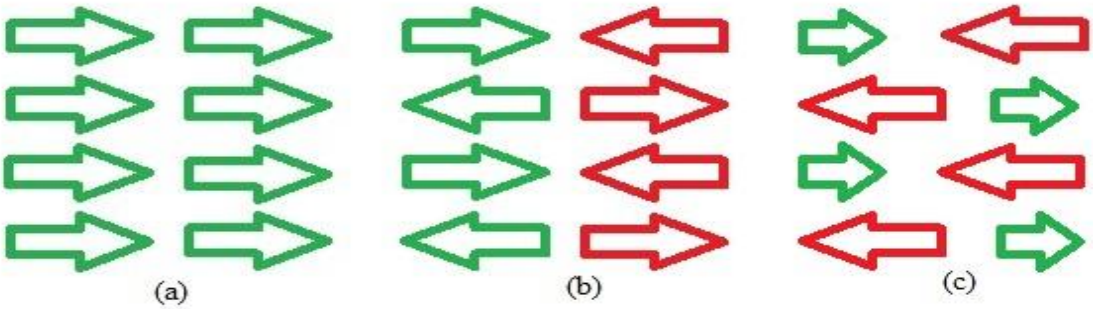

Fig. 1: Schematically illustrated coupled magnetic moments: (*a*) ferromagnetism, (*b*) antiferromagnetism, (*c*) ferrimagnetism.

In *ferromagnetic* (FM) materials a parallel alignment of magnetic moments can be observed below a characteristic temperature T_c, called the Curie temperature, causing spontaneous nonzero magnetization (see Fig. 1(*a*)). At temperatures $T > T_c$ these materials show paramagnetic behaviour and the susceptibility in this region follows the *Curie-Weiss law*:

$$\chi = \frac{C}{T - \theta_P} \tag{19}$$

where $\theta_P > 0$ is the paramagnetic Curie temperature. In a simple ferromagnet the exchange integral J is positive [3, 11].

The upper limit of parallel magnetic moment alignment in ferromagnetic materials is given by the saturated magnetization [8]. A typical development of magnetization in presence of applied magnetic field (hysteresis loop) is shown in Fig. 2. As the external magnetic field is applied, magnetization gets eventually saturated, with all magnetic moments aligned parallel in the material. When the applied field is weakened in the opposite direction after saturation and reaches the value of zero on the vertical axis, we call this intersection residual magnetization. After further weakening of the magnetic field in the opposite direction, magnetization becomes zero and this intersection with horizontal axis is called "*coercive force*".

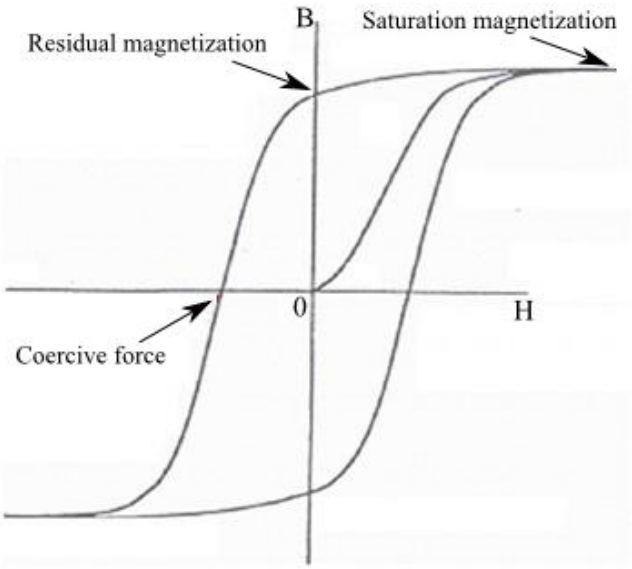

Fig. 2: Schematic hysteresis loop of a ferromagnetic material.

Metamagnetic phase transition can be observed on the hysteresis loop when a sufficient magnetic field is applied to materials which exhibit no or small spontaneous magnetization and consequently, an abrupt transition to high magnetization is induced. As it is a metastable state, it disappears when the field is removed [11].

Antiferromagnetics (AF) are characterized by an antiparallel alignment of magnetic moments (see Fig. 1(*b*)) below critical temperature T_N, called the Néel temperature [12]. At temperatures $T < T_N$ zero magnetization is observed due to mutual compensation of magnetic moments as shown in Fig. 3 (*b*). In the paramagnetic region, $T > T_N$ material follows the Curie-Weiss law with $\theta_P < 0$:

$$\chi \propto \frac{1}{T - \theta_P} \qquad (20)$$

In a simple antiferromagnet the exchange integral J is negative.

To sum up, the possible values for θ_P is 0 for a paramagnetic material; positive value of θ_P points to a ferromagnet where $\theta_P = T_c$ and negative value of θ_P is characterized as an antiferromagnet where the $\theta_P = - T_N$.

Ferrimagnetic materials (see Fig. 1(*c*)) belong to the nontrivial magnetically ordered systems (such as helicoidally and spirally ordered systems, spin glass etc.) [9, 10]. Ferrimagnetism can be described as uncompensated antiferromagnetism as shown

in Fig. 3(*c*); therefore nonzero spontaneous magnetization is observed below characteristic temperature.

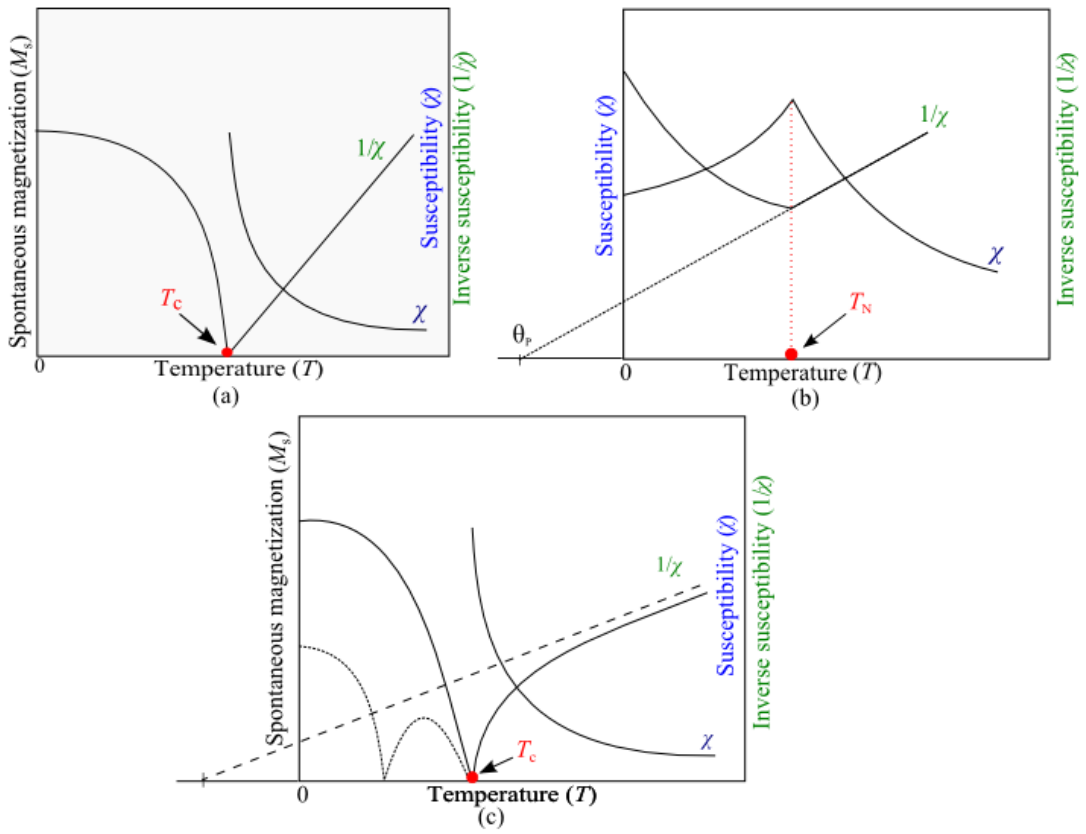

Fig. 3: Temperature dependence of susceptibility and inverse susceptibility: (*a*) ferromagnet, (*b*) antiferromagnet, (*c*) ferrimagnet – when magnetization of the *A* sublattice is significantly higher than magnetization of the *B* sublattice, the magnetization $M_s(T)$ resembles a ferromagnetic material (full line). The total magnetization given by different temperature dependences of the sublattice magnetizations is plotted using the dotted line.

2. Superconductivity

In many materials DC electrical resistivity suddenly drops to zero when reaching a characteristic temperature. This phenomenon called superconductivity (SC) was first observed by Heike Kamerlingh Onnes in 1911 in mercury [8]. Besides the fact that currents flow in a SC state with immeasurable dissipation [3], SC also reveals perfect diamagnetism [15, 43].

First phenomenological macroscopic theory explaining SC was proposed by V.L. Ginzburg and L. Landau in 1950 [35, 36]. Later, in 1957, a complete microscopic approach called BCS theory was proposed by J. Bardeen, L.N. Cooper and J.R. Schrieffer [16].

BCS theory describes the SC state as an ordered state of electron pairs called Cooper pairs which are formed due to electron-phonon interaction below an ordering temperature T_c [8].

So called conventional SC can be described within the BCS theory or its derivatives. Heavy fermion superconductors [20], cuprates, iron-based superconductors and organic superconductors form a new group of superconducting materials, whose behaviour needs to be described with a new approach. In these materials, it was suggested [18] that the spin-spin interactions can substitute the role of phonons [18, 19]. The conventional Cooper-pair is also known as the *s-wave* superconductivity carrier (see Fig. 4(*a*)). However in other magnetic systems close to magnetically ordered state one can expect a dominant spin-spin interaction and as a result, a new type of SC emerge – *p-wave* and *d-wave* state (see Fig. 4(*b*)) [18].

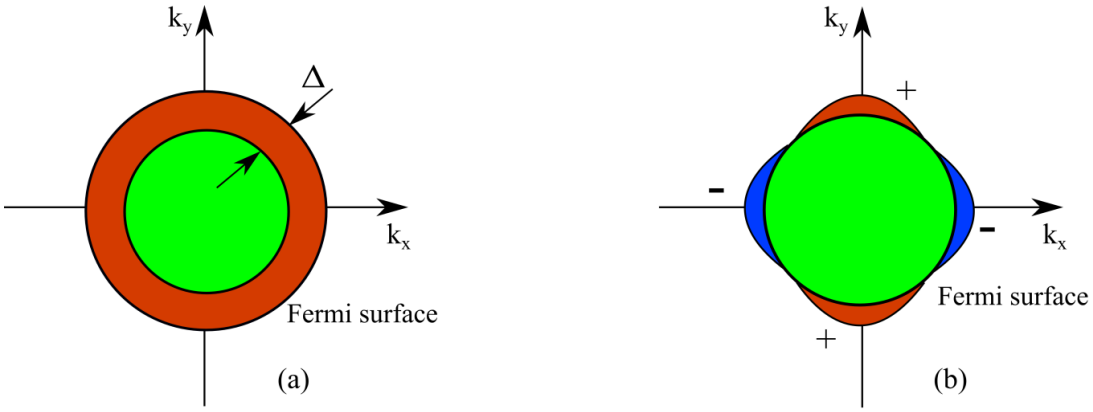

Fig. 4: (*a*) The scheme depicts an *s*-wave superconductor with isotropic gap; (*b*) *d*-wave superconductor with nods in *k*-space where the gap vanishes [18, 44].

3. Specific heat

Specific heat, a thermodynamic quantity, is defined as the amount of heat dQ required to raise the temperature T of a unit of mass in a unit of degree:

$$C_X(T) = \left(\frac{dQ}{dT}\right)_X \tag{21}$$

where X indicates a physical parameter which is kept constant during the measurement [30]. From experimental point of view the control parameter is usually pressure P. The specific heat can be expressed via entropy S:

$$C_P = T\left(\frac{\partial S}{\partial T}\right)_P \tag{22}$$

The specific heat C_P describes the entropy evolution of the system which is connected with the accessed energy levels due to thermal excitations. The total C_P can be written as a sum of individual contributions which become dominant at various temperature ranges [14].

Nuclear contribution C_{nuc} cannot be neglected at very low temperatures (T < 0.5 K) where it is usually recognized by a $C_{nuc} \sim T^{-2}$ dependence [13].

Conduction electron contribution C_{el} is usually dominant up to temperature 4 K. Theory describing C_{el} can be derived from the free electron gas using Fermi-Dirac distribution. It is defined as [8]:

$$C_{el} = \frac{1}{3}\pi^2 D(E_F) k_B^2 T = \gamma T \tag{23}$$

where $D(E_F)$ is the density of electronic states at the Fermi energy, γ is the Sommerfeld electronic factor which characterizes the proportionality between the electronic specific heat and the temperature. Since the Sommerfeld coefficient (typical values in mJ.mol^{-1}.K^{-2} range) is proportional to the density of states and therefore to the electron mass m_e, a further increase of this electronic term is observed in heavy fermions. The γ term becomes up to three orders of magnitude larger than that one of a simple metal [20].

Phonon specific heat contribution C_{pho} is a consequence of thermal lattice vibrations represented by quasiparticles called phonons. Phonons can be divided into $3n-3$ optical and *3* acoustic branches, where *n* is the number of atoms within a unit cell. The phonon contribution to the specific heat at low temperatures can be written as:

$$C_{pho} = \beta T^3 \qquad (24)$$

where $\beta = \frac{12}{5}\pi^4 R\left(\frac{1}{\theta_D}\right)^3$. The parameter θ_D is the Debye temperature characterizing acoustic branches in the quantum Debye-model [8].

In the high temperature region (around 300 K) the phonon contribution is independent on any material, and leads to the classical Dulong-Petit law:

$$C_{pho} = 3Nk_B \qquad (25)$$

where *3N* describes 3 degrees of freedom of *N* atoms.

In a magnetic system, another contribution to the specific heat, connected with magnetic order, C_{mag} has to be considered. Practically, C_{mag} is obtained by subtracting electron and phonon contributions from measured specific heat C_P:

$$C_{mag} = C_P - \left(C_{el} + C_{pho}\right) \qquad (26)$$

The temperature dependencies of C_P of magnetically ordered systems are given by the spin-wave theory and they depend mainly on the type of magnetic ordering and the dimensionality of the system [13].

According to the phenomenological Landau theory [1] a transition from a paramagnetic to a magnetically ordered state is a *2*nd order phase transition which is presented by a discontinuity in a specific heat. On the other hand, the *1*st order phase transition reveals a discontinuity in entropy. The jump in entropy gives a latent heat [19]. A typical example of a *1st* order phase transition is a transition to the superconducting state.

In the paramagnetic regime, the magnetic contribution can be usually described somewhat easier. It is given by the *Schottky paramagnetic contribution* C_{Sch} which is

connected with CF perturbation. The energy splitting caused by CF effect contributes to the specific heat and it is called Schottky anomaly. It is given by [31]:

$$C_{Sch} = \frac{R}{T^2}\left\{\frac{\sum_{i=0}^{n}\Delta_i^2 \exp\left(-\frac{\Delta_i}{T}\right)}{\sum_{i=0}^{n}\exp\left(-\frac{\Delta_i}{T}\right)} - \left[\frac{\sum_{i=0}^{n}\Delta_i \exp\left(-\frac{\Delta_i}{T}\right)}{\sum_{i=0}^{n}\exp\left(-\frac{\Delta_i}{T}\right)}\right]^2\right\} \qquad (27)$$

where R is the gas constant, n is the number of energy levels and Δ_i is the energy of the i^{th} level.

4. Experimental methods

4.1. Synthesis

From the thermodynamic point of view compounds can be divided into congruently and incongruently melting materials according to their melting. A congruently melting solid phase melts into a liquid phase with the same composition. On the other hand, a solid phase melts during the incongruent melting into a liquid with different composition and produces another solid phase which has a different composition than the original solid.

Phase diagram is a temperature-composition scheme showing conditions at which phases can coexist at the thermodynamic equilibrium as a function of temperature. It provides essential information for the crystal growth preparation. The binary phase diagrams consist of two elements and are available for most of the existing combinations of elements; generally, *n* elements lead to N-dimensional diagrams, which are more difficult to depict. Therefore, the ternary phase diagrams are usually known only for certain temperatures as so-called iso-thermal sections [40]. Boundary line between liquid and solid phases (see Fig. 5) is called *liquidus-solidus line* [17]. Whereas at the peritectic point (P) both liquid and solid phases transform into another solid phase, at the eutectic point (E) the liquid phase transforms into two different solid phases.

The purity of metals is expressed in percentages with the following notation 3N = 99.9 %, 4N5 = 99.995 % … etc. Ultra high purity materials (mainly transition metals, RE and their intermetallic compounds) can be prepared by Solid State Electrotransport (SSE). This method uses ultrahigh vacuum and large DC current at high temperatures (level of purity is then denoted by SSE) [32].

4.1.1. Polycrystalline materials

Polycrystalline materials show isotropic behaviour due to their randomly oriented grain structure and reveal periodicity only within small grains. Generally, their synthesis is not time-consuming neither complicated, therefore providing the opportunity to analyze basic physical properties. In some cases it is useful to anneal polycrystalline samples in order to achieve better homogeneity or to obtain the desired composition of the material by stabilization of incongruently melting phases [41].

4.1.2. Single crystals

The most important advantage of single crystals is a possibility to study the anisotropic properties of materials. In contrast to the polycrystalline materials, single crystals also provide higher purity and less grain boundaries. An extensive variety of crystal growth techniques has been developed to produce single crystals [34].

Fig. 5: The quartz ampoule containing the crucible with starting elements and the quartz wool.

Growth from melt is the most widely used technique of crystal growth. There are several methods using its principle such as:

Czochralski method (crystal pulling); a seed crystal is dipped into a melted environment and then slowly rotated and lifted to obtain a single crystal of the desired diameter and length. However, incongruently melting compounds with high vapor pressure cannot be prepared by this method.

Bridgman-Stockbarger techniques allow a steady motion of a freezing solid-liquid interface along an ingot. Either the whole ingot can be melted - normal freezing - or a molten zone is established – zone melting [33, 34].

Floating zone method does not require the use of any container and it is advantageous for materials with high surface tension and low density. There is an upper limit of crystal diameter and length ordered by gravitational forces [34].

Bulk single crystals can also be *grown from vapor phase* by sublimation, chemical transport or chemical vapor deposition [34]. These techniques are mainly used in silicon industry, growing thin layers of silicon or semiconductors.

Solution- or flux growth technique; Solution growth method is often used in material research. Its most distinct advantage is the possibility to prepare incongruently melting materials. Moreover, this method uses relatively simple equipment and consumes small amounts of starting elements. The single crystals

maintain their natural habit. The stoichiometry cannot be controlled during the crystal growth which often leads to presence of impurities. This fact puts a strain on a careful characterization of the growth products.

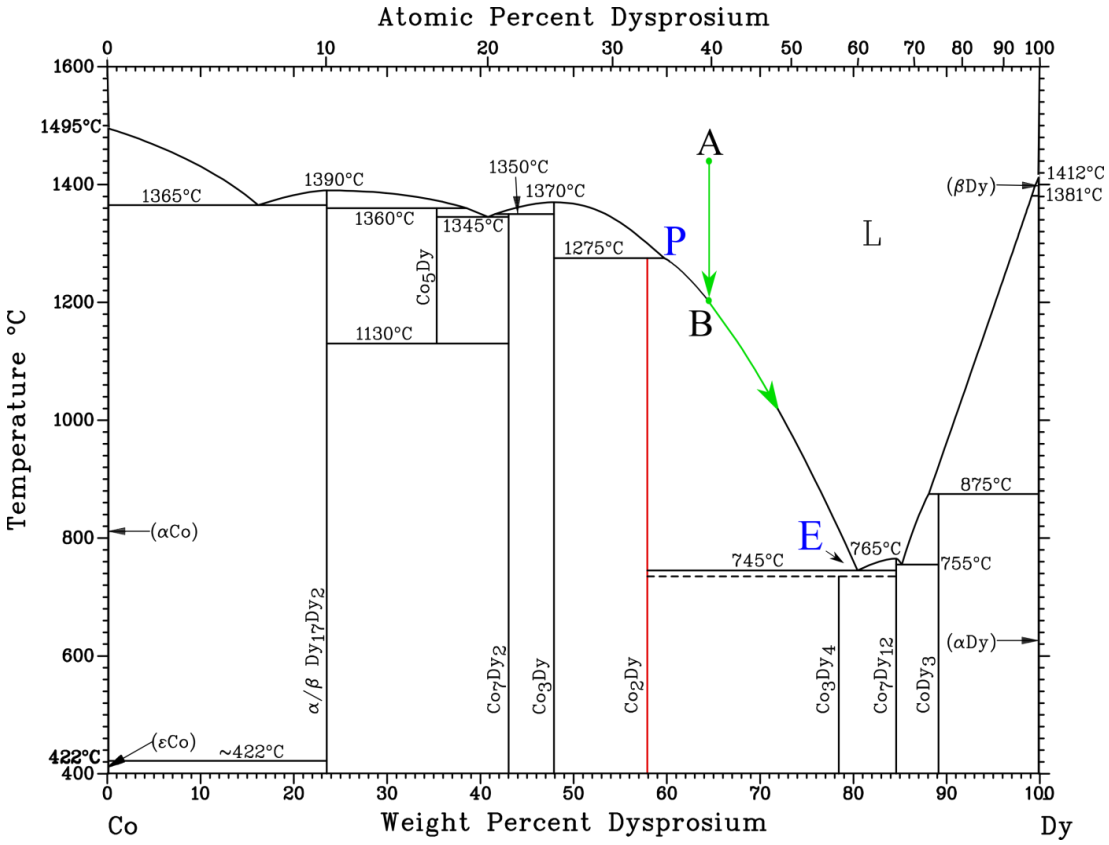

Fig. 6: The Dy-Co phase diagram. P marks the peritectic point of $DyCo_2$ phase and E marks the eutectic point. The vertical red line depicts the starting ratio of Dy and Co elements. The green arrows present the growth process of $DyCo_2$ phase.

The principle of solution growth method is explained on an example of the incongruently melting $DyCo_2$ compound which appeared in several batches prepared within this work. The Dy-Co phase diagram is presented in Fig. 6. According to this phase diagram the starting ratio of Dy:Co should not be lower than approx. 3:2 to prevent the growth of the unwanted phase $DyCo_3$. The starting composition is heated up to the point A (~ 1450 °C); then the cooling begins with a slow and constant rate. At the temperature 1200 °C (point B) the composition reaches the solidus-liquidus line; at this point the solution is saturated and the $DyCo_2$ single crystals start to grow. Solution becomes Dy-richer following the solidus-liquidus line (see the green curve in Fig. 6). The system is no longer homogenous; it contains a solid phase of one stoichiometry and liquid phase of another. The ratio of both phases is given by the

lever rule [34]. To avoid the growth of the Dy_4Co_3 phase, the cooling should be stopped above 745 °C. The residual flux can be decanted by a standard way [42].

Since the constituent elements at high temperatures tend to form oxides a protective environment is needed. First, the elements of stoichiometric amounts are placed in high quality alumina crucibles [67] after that the crucibles are sealed in an amorphous quartz ampoule (see Fig. 5) and the ampoules are evacuated down to a pressure ~ 10^{-6} mbar. Finally, the ampoules are placed in laboratory furnaces CLASIC 3013L [68].

4.2. Scanning electron microscope (SEM)

The measurements presented in this thesis were performed on Tescan Mira I LMH SEM [21], equipped with SE and BSE detector and with the energy dispersive *X*-ray analyzer Bruker AXS [22] (see Fig. 7).

Fig. 7: Tescan Mira I LMH scanning electron microscope with EDX analyzer.

Scanning electron microscope (SEM) uses a focused, high energy electron beam (usually units or tens of keV) to extract information (structural, chemical) from a desirable region of the sample. After the primary electrons (PE) emitted by the electron gun interact with the sample, a variety of signals is produced [37, 38]:

Secondary electrons (SE) are the result of ionization processes (< 50 eV). SE originate from inelastic interactions between primary electron beam and atoms near the surface of the sample. Therefore, the SE provide mainly the topographical information. The incident energy of the electron beam and the atomic number *Z* of the elements present in the sample are the most important factors which determine the interaction volume. Generally, the information from SE is obtained from a depth ~ 1 – 10 nm.

Backscattered electrons (BSE) are high energy electrons (>50 eV), reflected out of the sample as a result of inelastic scattering. The penetration depth of BSE corresponds approx. to the half of the penetration depth of the PE. BSE have worse resolution than secondary electrons; on the other hand, they are strongly dependent on the atomic number *Z*; thus, they provide information not just about the topology of the surface but primarily about the distribution of different elements in the sample. The areas containing heavier elements appear lighter, whereas areas containing lighter elements appear darker.

Characteristic X-rays are used to identify the chemical composition of the sample. EDX spectroscopy is based on the *X*-ray excitations of the sample. Every element has a unique atomic structure; therefore interaction of high energy electrons with the sample allows a unique set of peaks on its spectrum [26]. The penetration depth of characteristic *X*-rays corresponds nearly to the penetration depth of the PE; thus it is a suitable probe for composition determination. EDX analysis allows the user different types of scanning methods, to extract information of a desirable area. Point scan determines the composition of a material in a small area corresponding to the diameter of the electron beam. The line scan determines the concentration of elements along a selected line segment and the mapping scan provides qualitative information creating a 2D map which reveals inhomogeneities and impurity phases easily.

4.3. *X*-ray diffraction methods

Laue method

Laue method is a rapid experimental technique used mainly to determine the orientation and quality of single crystal samples. A continuous *X*-ray spectrum emitted from Cu lamp is reflected from (back-reflection Laue method), or transmitted through (transmission Laue method) a fixed crystal. The diffraction pattern is produced if a correct wavelength that satisfies the Bragg law [26] is contained in the continuous spectrum of used radiation. In the case of back-reflection Laue method diffraction spots lie generally on a hyperbola.

The Laue patterns were taken on the basis of back-reflection method on Micrometa 600 apparatus using polychromatic Cu *X*-ray radiation. Diffraction patterns were collected on a plane film with 10 cm radius, placed 3 cm apart from the sample.

Powder diffraction

X-ray powder diffraction (XRD) is analytical technique primarily used for structure and phase characterization of single- and polycrystalline materials. The crystal structure can be determined using specialized techniques such as Rietveld refinement [26, 27]. For the crystal structure determination FullProf software was used. The program is based on the method of least squares. It can be used as a profile matching tool for both qualitative and quantitative analysis, with or without the

knowledge of the actual crystal structure. It can also simulate the desired crystal structures [39].

Single crystal samples prepared within this work were powdered into a fine powder and uniformly distributed on silicon plate. Diffraction measurements were performed primarily on Bruker D8 Advance diffractometer [22] with Bragg-Brentano $\theta - 2\theta$ geometry [26] and monochromatic Cu K_α radiation with wavelength $\lambda = 1.540562$ Å. Selected samples were also measured at the High-resolution Powder-diffraction Beamline ID31 at the European Synchrotron Radiation Facility (ESRF), Grenoble [46]. Used wavelength of the incident photon beam was 0.40007(2) Å.

4.4. Specific heat and magnetic measurements

The specific heat, magnetic and AC/DC susceptibility measurements were performed in Joint Laboratory for Magnetic Studies [23] (JLMS) using PPMS (Physical Property Measurement System) and MPMS/SQUID (Magnetic Property Measurement System/ Superconducting Quantum Interference Device) from Quantum Design, Inc [24, 25]. Measurements were performed in the temperature range of 1.8-300 K in magnetic fields up to 9 T, 14 T and 7 T on PPMS 9 T, PPMS 14 T and MPMS 7 T, respectively. The PPMS apparatus is equipped with a Helium-3 system which enables to operate in the low temperature region (T > 0.35 K). Helium-3 insert is compatible with the heat capacity, resistivity and AC transport measurement options [25]. Even lower temperatures can be achieved by recently installed dilution refrigerator [23] designed for temperatures below 0.05 K with simultaneous application of a magnetic field up to 9 T.

4.5. Computational methods

The method applied on the RE_2CoIn_8 compounds is density functional theory (DFT) [96] within local density approximation (LDA) [96] and generalized gradient approximation (GGA) [97, 98]. For this purpose, two independent computational methods, namely the full potential augmented plane wave plus local orbitals method (APW-lo) and full potential local-orbital method (FPLO) were used to solve the single particle Kohn-Sham equations [2] (for more details see Ref. [62]).

Density functional theory is a quantum mechanical method used to investigate the electronic structure of many body systems. The basic idea of DFT is that the

energy of an electron system can be given by the electron probability density ρ. Its advantage is a little computational cost compared to other ab initio calculations such as Hartree-Fock method. Classical DFT is based on solution of Kohn-Sham equations. Kohn-Sham potential takes into account electron exchange-correlation term. As we do not know this exchange-correlation potential of a general system exactly, we use approximate expressions instead of it. The most widely used approximation is LDA; the functional depends only on density at the coordinate where the functional is evaluated. GGA represents a numerical approximation which takes into account also the gradient of the density at the same coordinate.

The APW method solves Kohn-Sham equations not only close to nucleus but also in the interstitial region. The space of the unit cell is divided into spheres centered in each atom site and into the interstitial region. In the APW + lo method local orbitals (lo) are included to improve the APW basis.

5. Selected compounds for physical studies

All ternary indides studied in this work belong to the family of compounds represented by a general formula $RE_nT_m\mathrm{In}_{3n+2m}$ (*RE* = rare earth, *T* = transition metal). $RE_nT_m\mathrm{In}_{3n+2m}$ compounds crystallize in the $\mathrm{Ho}_n\mathrm{Co}_m\mathrm{Ga}_{3n+2m}$ tetragonal structure with the space group P4/mmm (see Tab. 1) except for compounds with n = 1, m = 2 where the space group is I4/mmm. The crystal structure consists of m layers of $T\mathrm{In}_2$ alternating with n layers of CeIn_3 along the tetragonal c-axis (see Fig. 8).

The arrangement of the rare earth atoms is purely three-dimensional (3D) for the cubic compounds, whereas it takes a quasi two-dimensional (2D) character for the tetragonal compounds in the sequence $RE_3T\mathrm{In}_{11} - RE_5T_2\mathrm{In}_{19} - RE_2T\mathrm{In}_8 - RET\mathrm{In}_5$ with the strongest 2D character in the $RET_2\mathrm{In}_7$ structure. The compounds are according to their stoichiometries often simply called “115”, “218” and “127”. For the two new Pd compounds [40] we use the abbreviations “3-1-11” and “5-2-19”. Such a large group of structurally related compounds gives a great opportunity for systematic investigations of electronic properties and their relationship with dimensionality for various *RE* and *T* metals. Tab. 1 summarizes structure parameters of cerium compounds for different values of *n* and *m*.

m	***n***	**Phase formula**	**Space group**	**Cell parameters**	
				a **(Å)**	***c*** **(Å)**
0	1	CeIn_3 [64]	Pm-3m	4.6894(2)	-
1	3	$\mathrm{Ce}_3\mathrm{PdIn}_{11}$ [40]	P4/mmm	4.6846(8)	16.846(8)
2	5	$\mathrm{Ce}_5\mathrm{Pd}_2\mathrm{In}_{19}$ [40]	P4/mmm	4.70120(10)	29.1359(4)
1	2	$\mathrm{Ce}_2\mathrm{PdIn}_8$ [78]	P4/mmm	4.6931(2)	12.2048(7)
		$\mathrm{Ce}_2\mathrm{RhIn}_8$ [73]		4.66325(18)	12.23875(51)
		$\mathrm{Ce}_2\mathrm{CoIn}_8$ [50]		4.640	12.251
		$\mathrm{Ce}_2\mathrm{IrIn}_8$ [74]		4.6897(6)	12.1950(11)
1	1	CeRhIn_5 [69]	P4/mmm	4.652	7.544
		CeCoIn_5 [61]		4.601(1)	7.540(2)
		CeIrIn_5 [70]		4.673(1)	7.505(3)
2	1	$\mathrm{CePt}_2\mathrm{In}_7$ [71]	I4/mmm	4.6093(2)	21.627(1)

Tab. 1: Structure parameters of $\mathrm{Ce}_nT_m\mathrm{In}_{3n+2m}$ intermetallic compounds.

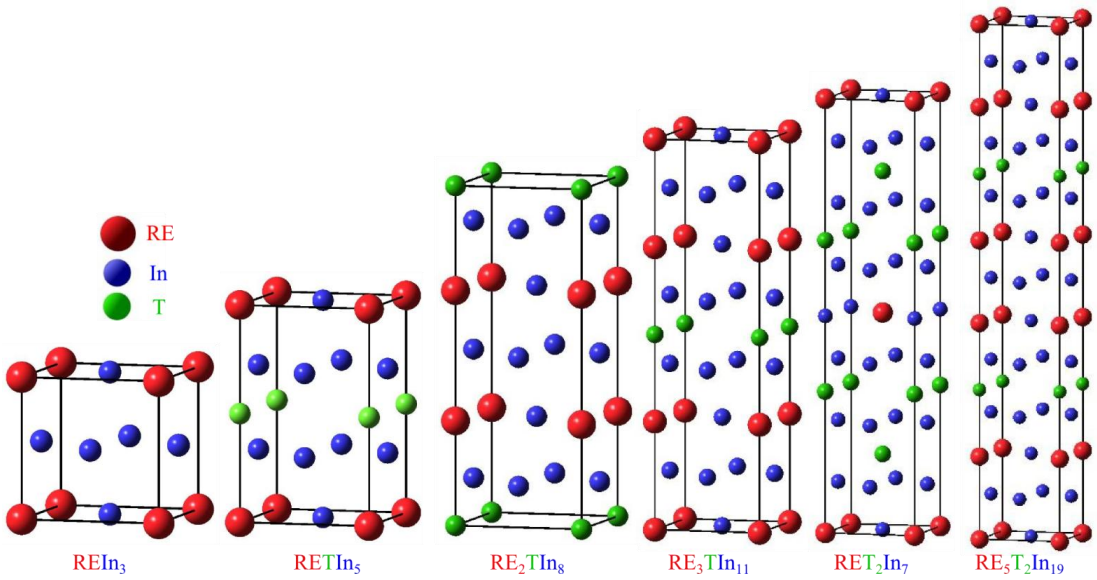

Fig. 8: Primitive cells of $RE_nT_m\mathrm{In}_{3n+2m}$ crystal structure for various *n* and *m*.

5.1. Non-cerium $RE_2\mathrm{CoIn}_8$

After discovery of the heavy fermion superconductivity in $\mathrm{Ce}_2T\mathrm{In}_8$ and $\mathrm{Ce}T\mathrm{In}_5$ (T = Co, Rh, Ir) [51, 72], the compounds with the $\mathrm{Ho}_n\mathrm{Co}_m\mathrm{Ga}_{3n+2m}$-type tetragonal crystal structure have attracted strong interests in this field. As the superconductivity in these compounds is presumably magnetically mediated, studies of non-Kondo isostructural materials are crucial to understand the evolution of their magnetic properties given by the *f*-electrons. $RE_2\mathrm{CoIn}_8$ compounds crystallizing in $\mathrm{Ho}_2\mathrm{CoGa}_8$ structure type (see Fig. 8) [61] reveal various magnetic orderings and metamagnetic transitions [1]. The compounds were also studied theoretically by calculations from first principles based on the density functional theory (DFT) [62]. $\mathrm{Pr}_2\mathrm{CoIn}_8$ was found to be a Van Vleck paramagnet. For the $\mathrm{Nd}_2\mathrm{CoIn}_8$ and $\mathrm{Dy}_2\mathrm{CoIn}_8$ compounds the CF splitting was calculated and the obtained parameters of CF Hamiltonian predict the anisotropy of the magnetic properties of these materials in the single crystal form.

The polycrystalline samples of $RE_2\mathrm{CoIn}_8$ were experimentally studied by means of magnetic, thermal and transport measurements down to 2 K [50]. As this study is focused on $RE_2\mathrm{CoIn}_8$, where RE = Pr, Nd and Dy, we would describe these compounds in more detail.

$\mathrm{Pr}_2\mathrm{CoIn}_8$ reveals a dominating CF effect at low temperatures. No magnetic ordering down to 2 K in the resistivity measurements and the linear magnetic isotherm point to paramagnetic behaviour of $\mathrm{Pr}_2\mathrm{CoIn}_8$ [50].

The magnetic susceptibility and specific heat measurements of Nd_2CoIn_8 compound point to an antiferromagnetic transition at 10 K which broadens and shifts to lower temperatures in magnetic fields as expected in the AF case. A metamagnetic transition is observed at 2 K in the magnetic field of 6 T. The magnetoresistance curve shows a downward turn indicating the onset of FM behaviour above 8 T [50].

The susceptibility and specific heat measurements of Dy_2CoIn_8 compound reveal an antiferromagnetic transition at T_N = 17.4 K. Another magnetic transition observed at 5 K might be caused by a reorientation of the spin. In higher magnetic field, the transition at 17.4 K broadens and shifts to lower temperatures while the latter transition disappears completely. The $M(H)$ curves reveal two metamagnetic transitions at 3.8 and 8.2 T at temperatures below the Néel temperature (see Fig. 9). According to the magnetization and magnetoresistance data, the second metamagnetic transition transfers Dy_2CoIn_8 into the ferromagnetic state [50].

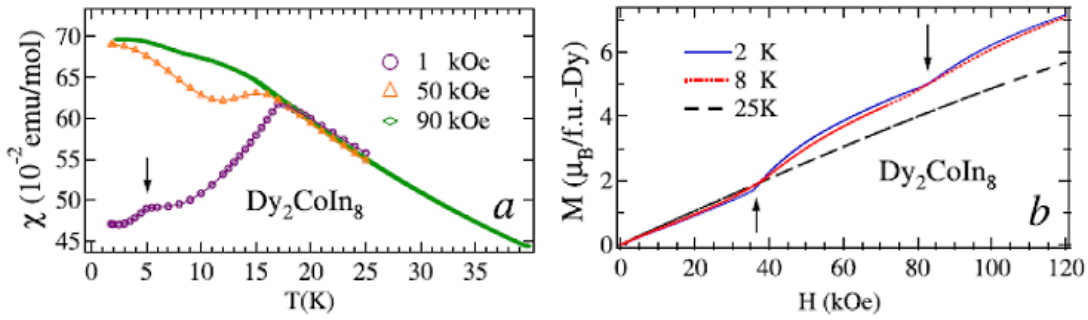

Fig. 9: Magnetization measurements of Dy_2CoIn_8. After Joshi *et al.*[50].

Magnetic susceptibility of the non-magnetic Y_2CoIn_8 compound shows behaviour characteristic for a Pauli paramagnet. The other compounds with *RE* = Nd, Sm, Gd, Tb, Dy and Ho reveal antiferromagnetic ordering below T_N = 10, 12, 33.5, 30, 17.4 and 7.6 K, respectively [50].

5.2. $Ce_nT_mIn_{3n+2m}$ (T = Co, Ir, Rh, Pd, Pt)

Ce compounds within the $RE_nT_mIn_{3n+2m}$ family have been a subject of intensive studies for more than one decade. As they exhibit enhanced effective mass of conduction electrons, a large variety of unusual physical properties such as non-Fermi liquid (NFL) behaviour [49] and quantum criticality [60] can be investigated. Unconventional superconductivity emerges in the vicinity of the materials' quantum critical point (QCP) and interplay between magnetism and SC is observed [51, 79]. However, this family of compounds is interesting for some other reason. As the tetragonal structures in these compounds provide the possibility to tune the structural dimensionality, this makes them ideal candidates to investigate the influence of the parameter "dimensionality" with respect to quantum criticality [75].

The ground state physical properties – the SC transition temperature T_c, Néel temperature T_N and the critical pressure P_c (where the AF state vanishes and T_N extrapolates to zero temperature) of $Ce_nT_mIn_{3n+2m}$ compounds are listed in Tab. 2.

Phase formula	T_c **(K)**	T_N **(K)**	P_c **(GPa)**
$CeIn_3$ [52, 91]	0.19	10.2	2.65
$CeCoIn_5$ [50, 51]	2.3	-	-
Ce_2CoIn_8 [50]	0.4	-	-
$CeIrIn_5$ [54]	0.4	-	-
Ce_2IrIn_8 [65]	PM down to 50 mK	-	-
$CeRhIn_5$ [10, 51, 57]	2.12	3.8	1.7
Ce_2RhIn_8 [51, 57]	0.9	2.8	2.5
Ce_2PdIn_8 [63]	0.69	-	-
Ce_3PdIn_{11} [40]	PM down to 1.72 K	-	-
$Ce_5Pd_2In_{19}$ [40]	PM down to 1.72 K	-	-
$CePt_2In_7$ [76, 77]	2.1	5.5	3.5

Tab. 2: Basic physical properties of $Ce_nT_mIn_{3n+2m}$ compounds.

The synthesis of the heavy-fermion superconductor, Ce_2PdIn_8 was first reported by Shtepa *et al.* [78]. *X*-ray powder diffraction of polycrystalline samples of Ce_2PdIn_8 revealed the Ho_2CoGa_8-type (see Fig. 8) with the P4/mmm space group [78].

As other $Ce_nT_mIn_{3n+2m}$ compounds [65, 81] Ce_2PdIn_8 single crystals have been prepared by the self-flux method [63, 72]. However the synthesis appeared to be very complicated as controversial results have been published, depending on sample preparation. First results on polycrystalline Ce_2PdIn_8 have shown paramagnetic behaviour down to 0.35 K [72] with NFL behaviour below 6 K, while later superconductivity was observed below T_c ~ 0.7 K in a single crystal sample [87, 88, 89]. After that, also polycrystals annealed at 700 °C showed superconducting transition below 0.7 K [50, 78]. Moreover, the compound has strong tendency to grow in a sandwich-like system on top of $CeIn_3$ single crystals [63]. However, other question arised from the origin of the anomaly at T_t = 1.7 K, which has been shown only once [90] while polycrystalline samples [40, 50] and crystals prepared from Pd-rich solution [63] do not show such anomaly. Pressure studies [86] up to 2.1 GPa show that increasing pressure gradually suppresses T_c and pushes the system away from the NFL state. Various methods (nuclear quadrupole resonance [83], thermal conductivity [82], magnetoresistivity [84]) used to investigate the compound in recent years, indicate that the Ce_2PdIn_8 is close to the AF QCP, and the SC state has an unconventional character emerging near QCP.

Ce_3PdIn_{11} and $Ce_5Pd_2In_{19}$ represent new structure types in the $RE_nT_mIn_{3n+2m}$ family of compounds [40] (see Fig. 8). Magnetic measurements of polycrystalline compounds carried out in 1.72 – 400 K temperature range revealed that they are both Curie-Weiss paramagnets with no hint of magnetic ordering down to the lowest temperature. Their magnetic and electrical properties yield similar features as Ce_2PdIn_8 compound, therefore their investigation in ultra-low temperature region is necessary.

$CePt_2In_7$ represents a new structure type with I4/mmm space group and the strongest 2D character from the compounds of $Ce_nT_mIn_{3n+2m}$ family [71] (Tab. 1). Investigation of polycrystals of $CePt_2In_7$ [77] revealed antiferromagnetic ordering below T_N = 5.5 K. From the specific heat measurements, the Sommerfeld coefficient γ = 340 $mJ.mol^{-1}.K^{-2}$ was obtained, indicating a HF behaviour. Hydrostatic pressure studies revealed pressure-induced superconductivity in pressure range from 1 to 3 GPa coexisting with AF order. The NQR studies indicate that the antiferromagnetism is commensurate in $CePt_2In_7$ [85].

6. Results and discussion

6.1. RE_2CoIn_8 (RE = Dy, Nd, Pr)

6.1.1. Synthesis

Single crystalline samples of RE_2CoIn_8 were grown from In flux, using high purity elements (Dy 4N, Nd 4N, Pr 3N, Co 4N5 and In 5N). The glass tubes with the batches placed in alumina crucibles were heated up (rate ~ 200 °C/h) to the maximum temperature, kept there for several hours (8 – 10 h) to let the homogenization take place and then cooled down with a slow rate (3.3 – 4.5 °C/h) and decanted. The final conditions for the growth of 218 phases are results of several attempts. The first procedure similar to those described in the case of other $RE_2T\text{In}_8$ compounds [80] led to production of merely 115 single crystals with no traces of other ternary phases. We shifted the temperature range to higher values well above the liquidus-solidus line in the Pr-Co diagram to find out if it would be possible to omit the growth of the 115 phase. The growth of ternary phase was avoided; however, only the binary phase $PrIn_3$ was obtained. These unsuccessful attempts brought us to a conclusion to perform our experiments in lower temperature ranges to avoid the growth of both binary and 115 phases. We used non-integer starting compositions with a surplus of RE elements to move further in the binary phase diagram to the a region closer to binary compounds with RE:Co ratio > 2 (see the red line in Fig. 10). As a result of the growth process plate like single crystals of typical sizes of ~ 1 mm × 1 mm × 0.5 mm were obtained (see Fig. 11).

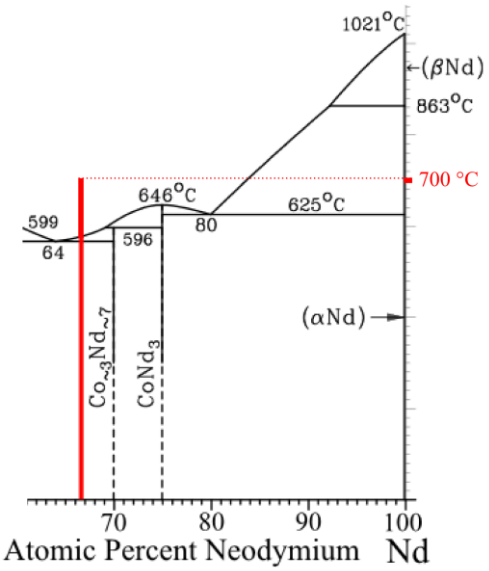

Fig. 10: The Nd-rich section of the Nd-Co binary phase diagram.

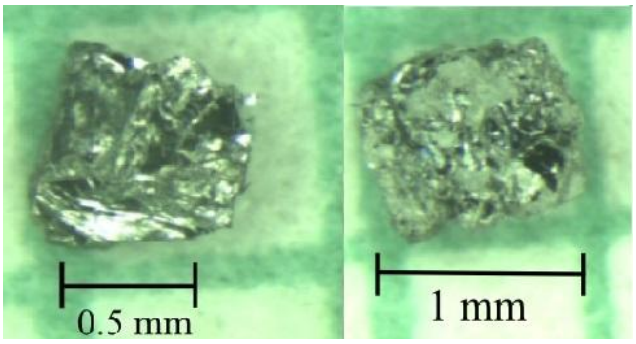

Fig. 11: Single crystals of RE_2CoIn_8 obtained from In flux.

The final growth conditions as a result of several attempts as well as the obtained final products are listed in Tab. 3.

RE	**Starting composition (*RE*:Co:In)**	**Temperature range (°C)**	**Final products**
Pr	2.2:1:50	700 – 300	Pr_2CoIn_8
	2:1:35	950 – 650	$PrIn_3$
	2:1:40	900 - 350	$PrCoIn_5$
Nd	2.15:1:50	700 – 300	Nd_2CoIn_8
	2:1:40	900 – 350	$NdCoIn_5$
Dy	2:1:50	770 – 300	Dy_2CoIn_8, $DyCoIn_5$
	2.15:1:50	820 – 300	Dy_2CoIn_8
	2:1:40	900 – 350	$DyCoIn_5$

Tab. 3: Growth conditions of RE_2CoIn_8 compounds.

6.1.2. Characterization

Energy dispersive *X*-ray analysis was performed on randomly selected crystals from the batches in order to determine the actual composition and homogeneity of the sample (see Tab. 4).

Pr_2CoIn_8		**Nd_2CoIn_8**		**Dy_2CoIn_8**	
Pr	18.6 ± 0.7	Nd	19.1 ± 0.7	Dy	18.0 ± 0.6
Co	9.5 ± 0.5	Co	9.6 ± 0.9	Co	9.6 ± 0.6
In	71.9 ± 0.8	In	71.3 ± 1.4	In	72.4 ± 1.1

Tab. 4: Results of EDX point scan analyses with standard deviation.

For EDX scanning, samples were smoothly polished using diamond discs with grains of sizes from 3 μm to 0.1 μm. In all RE_2CoIn_8 compounds the EDX point scans (see Tab. 4) as well as the mapping scan (see Fig. 12 and Fig. 13) revealed good homogeneity of the 218 samples. In the case of Nd_2CoIn_8 the measurement time was approx. 30 minutes whereas the measurement of Pr_2CoIn_8 sample lasted over 3 hours. Mapping scans of Dy_2CoIn_8 (not shown) revealed also very good homogeneity of the studied phase.

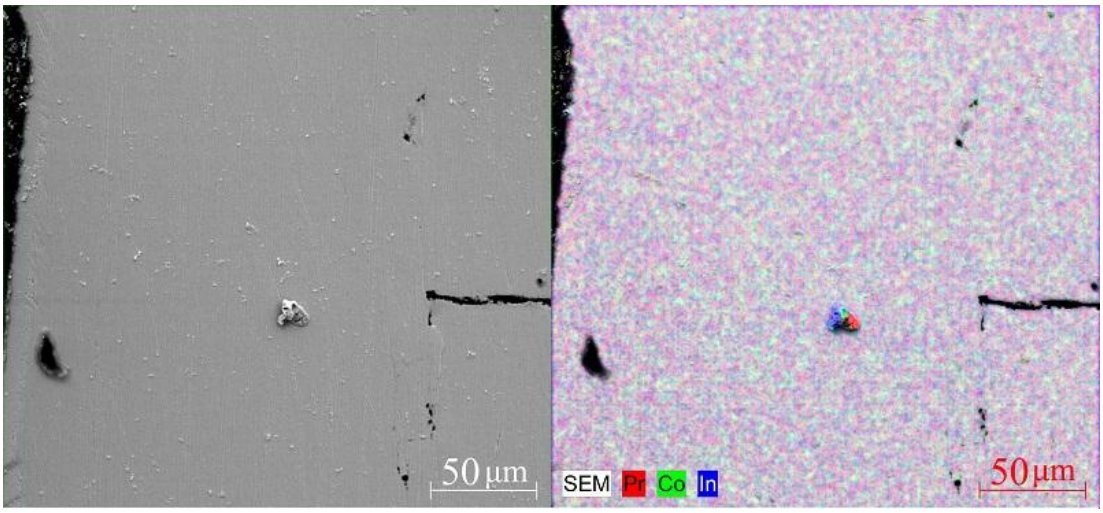

Fig. 12: The left-hand side depicts the selected area of the sample in SE detector 700-times magnified. SEM image with elements mapping of the surface of the Pr_2CoIn_8 sample is shown on the right-hand side.

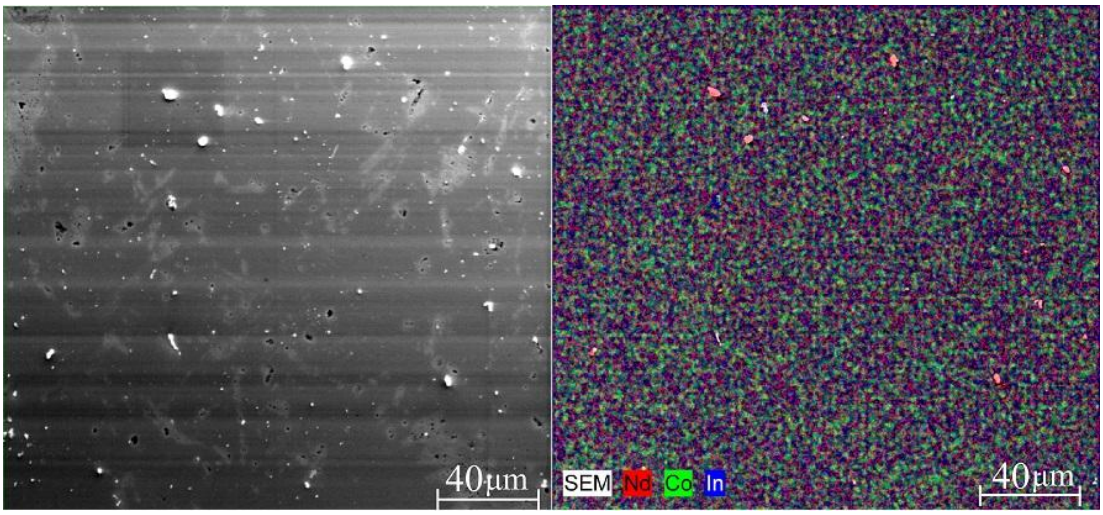

Fig. 13: The selected area of the sample in SE detector 800-times magnified is shown on the left. SEM image with elements mapping of the Nd_2CoIn_8 sample is shown on the right.

To check the structure and purity of the phases, powder *X*-ray diffraction was performed on powdered single crystals selected from the batches (see Fig. 14). The *X*-ray analysis confirmed Ho_2CoGa_8 crystal structure type with the space group P4/mmm for all measured samples. The cell parameters and atomic coordinates are listed in Tab. 5 and Tab. 6 and they are compared with previously published results [50]. The cell parameters obtained from the analysis of the polycrystalline samples [50] provide results analogous to the parameters from this work. In all of the cases the resemblance is approx. 99%.

RE_2CoIn_8	Cell parameters		Cell parameters [50]	
	***a* (Å)**	***c*(Å)**	***a* (Å)**	***c*(Å)**
Pr_2CoIn_8	4.663(1)	12.214(1)	4.615	12.193
Nd_2CoIn_8	4.613(7)	12.181(9)	4.608	12.172
Dy_2CoIn_8	4.556(3)	12.015(1)	4.561	11.99

Tab. 5: Lattice parameters of the studied RE_2CoIn_8 compared to the unit cell parameters published by Joshi *et al.* [50]

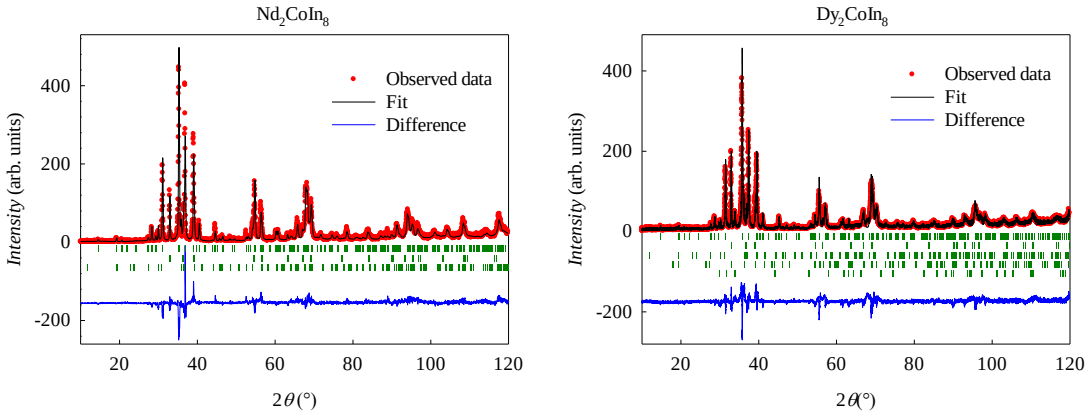

Fig. 14: Powder diffraction patterns of Nd_2CoIn_8 and Dy_2CoIn_8. Vertical green bars show the Bragg positions of the present phases and the blue line depicts the difference between the measured data (red points) and calculated fit (black line).

Compound	**Wyckoff pos.**	***x***	***y***	***z***	***z*** [50]
Pr_2CoIn_8					
Pr	2*g*	0.0	0.0	0.299(5)	0.306
Co	1*a*	0.0	0.0	0.0	0.0
In1	4*i*	0.0	0.5	0.118(6)	0.107
In2	2*h*	0.5	0.5	0.313(7)	0.308
In3	2*e*	0.0	0.5	0.5	0.5
Nd_2CoIn_8					
Nd	2*g*	0.0	0.0	0.305(5)	0.306
Co	1*a*	0.0	0.0	0.0	0.0
In1	4*i*	0.0	0.5	0.117(0)	0.107
In2	2*h*	0.5	0.5	0.309(1)	0.308
In3	2*e*	0.0	0.5	0.5	0.5
Dy_2CoIn_8					
Dy	2*g*	0.0	0.0	0.299(6)	0.306
Co	1*a*	0.0	0.0	0.0	0.0
In1	4*i*	0.0	0.5	0.119(5)	0.107
In2	2*h*	0.5	0.5	0.316(9)	0.308
In3	2*e*	0.0	0.5	0.5	0.5

Tab. 6: Atomic coordinates of RE_2CoIn_8 compounds compared to the coordinates published by Joshi *et al.* [50].

The Rietveld refinement of the *X*-ray powder diffraction patterns was performed on the basis of all present phases in order to include every observed peak. The phases used to fit all the reflections observed in the Dy_2CoIn_8 pattern are (Bragg positions in Fig. 14 from top to bottom): Dy_2CoIn_8, $DyCoIn_5$, $DyIn_3$ and Dy. The phases used for fitting the Nd_2CoIn_8 diffraction pattern are (from top to bottom): Nd_2CoIn_8, In and $NdCoIn_5$. The different phases and their weight fractions are listed in Tab. 7.

Pr_2CoIn_8 batch	**Fract. (%)**	**Nd_2CoIn_8 batch**	**Fract. (%)**	**Dy_2CoIn_8 batch**	**Fract. (%)**
Pr_2CoIn_8	69.2	Nd_2CoIn_8	78.1	Dy_2CoIn_8	73.9
$PrCoIn_5$	16.8	$NdCoIn_5$	13.4	Dy_3In	13.2
In	14.1	In	8.0	$DyCoIn_5$	7.9
-	-	-	-	Dy	3.6
-	-	-	-	In	1.6

Tab. 7: Quantitative analysis of the diffraction patterns.

Laue patterns were taken to verify the orientation of the single crystals. Laue pattern of the Pr_2CoIn_8 single crystal exposed for 50 min. is shown in Fig. 15. Laue patterns of other studied compounds (Nd_2CoIn_8, Dy_2CoIn_8) were analogous to the Pr_2CoIn_8 pattern.

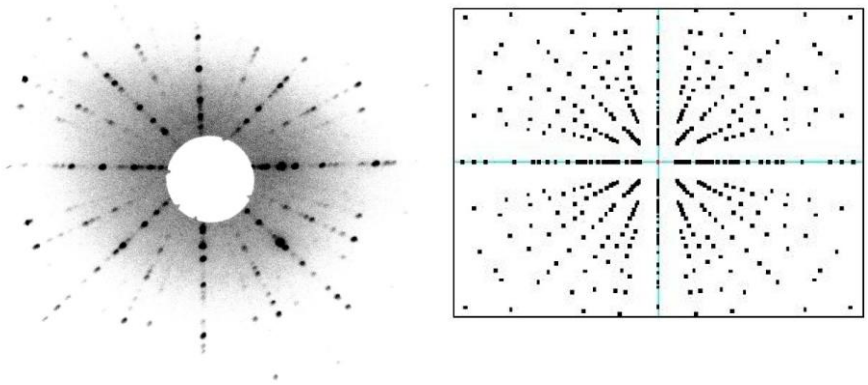

Fig. 15: The Laue pattern of the single crystal of Pr_2CoIn_8 used for further bulk measurements with its *c*-axis oriented perpendicular to the image plane is shown on the left-hand side. A corresponding simulated Laue pattern for Pr_2CoIn_8 crystal structure is shown on the right-hand side.

The single crystals corresponding to the requested stoichiometry, structure and purity were used for further bulk measurements.

6.1.3. Physical properties

Pr_2CoIn_8

The inverse susceptibility of Pr_2CoIn_8 is a linear function of temperature in the high temperature region but in the low temperatures it becomes nearly temperature independent as shown in Fig. 16. The ground state remains non-magnetic to the lowest measured temperatures T ~ 2 K and a temperature independent Van Vleck paramagnetism is observed.

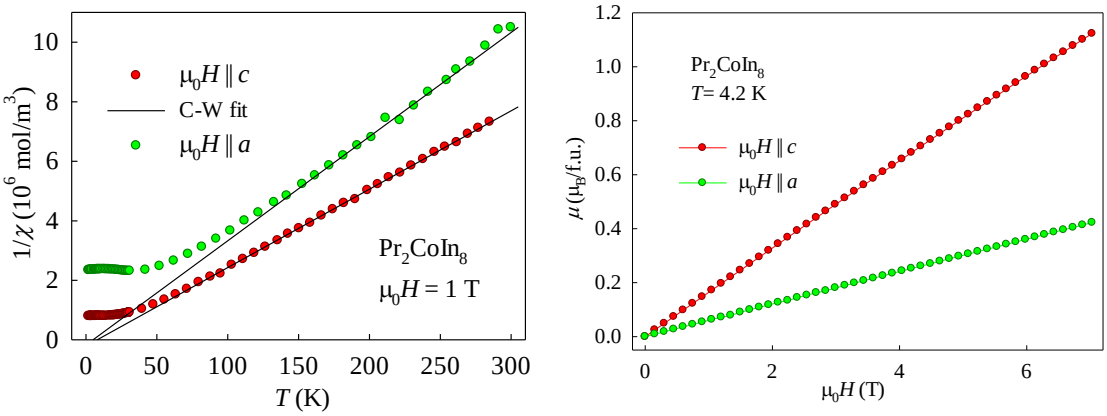

Fig. 16: Inverse susceptibility for the Pr_2CoIn_8 compound and the Curie-Weiss fit is shown on the left-hand side. Magnetic isotherm is shown on the right-hand side.

The *c*-axis is the easy axis in case of Pr_2CoIn_8, similarly to its 115 analog, as shown in the magnetization measurements in Fig. 16. The easy axis is the direction of magnetic moments preferred by the anisotropy energy. This energy is generally induced by the exchange and CF interactions [8]. The easy axis is different from the one obtained from theoretical calculations [62] (see Fig. 17).

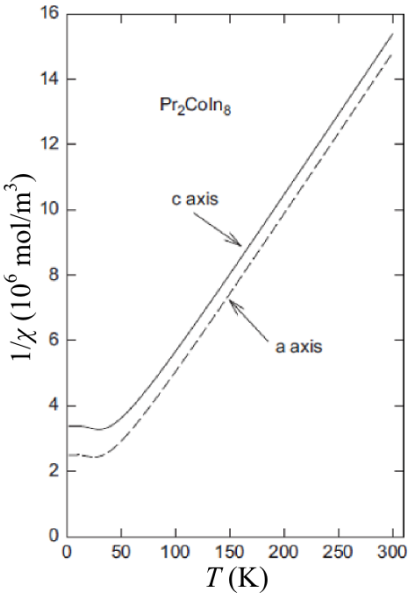

Fig. 17: Theoretical results by M. Diviš [62].

In $PrCoIn_5$ the *c*-axis susceptibility is 5-times higher than the *a*-axis susceptibility [92], while in the case of Pr_2CoIn_8 it is only by factor of ~ 3. This result is in agreement with the fact that the RE_nTIn_{3n+2} structures become less 2D-ike with increasing n and therefore the

anisotropy is lower for 218 compounds. The Curie-Weiss was performed in a temperature range from 100 K up to 300 K. The paramagnetic Curie temperatures θ_P are very close for both directions of the applied magnetic field compared to $PrCoIn_5$ indicating again lower anisotropy in the 218 system. The polycrystalline average of the effective moments gives much lower value 3.10 μ_B than expected for the free ion of Pr^{3+} (3.58 μ_B [8]). This fact points to a significant influence of the crystal field.

RE_2CoIn_8	μ_{eff} (μ_B/RE^{3+})			θ_P (K)		
	$\mu_0 H \parallel a$	$\mu_0 H \parallel c$	Joshi *et al.*[50]	$\mu_0 H \parallel a$	$\mu_0 H \parallel c$	Joshi *et al.*[50]
Pr	3.0	3.2	-	0	16	-
Nd	3.0	3.3	3.6	13	8	-12
Dy	10.5	10.6	10.6	-33	-17	-11

Tab. 8: The experimental values of the effective moments μ_{eff} and paramagnetic Curie temperatures θ_P for the studied RE_2CoIn_8 compounds.

Nd_2CoIn_8

The magnetic measurements revealed phase transition at around 10 K in accordance to previously published measurements [50]. The peak shifts to lower temperatures with the increase of the magnetic field; such behaviour is characteristic for an antiferromagnetic ground state. As the temperature independence of the inverse susceptibility is linear in a broad temperature region, the data can be fitted using the Curie-Weiss law (see Fig. 18) in the range from 100 K to 300 K.

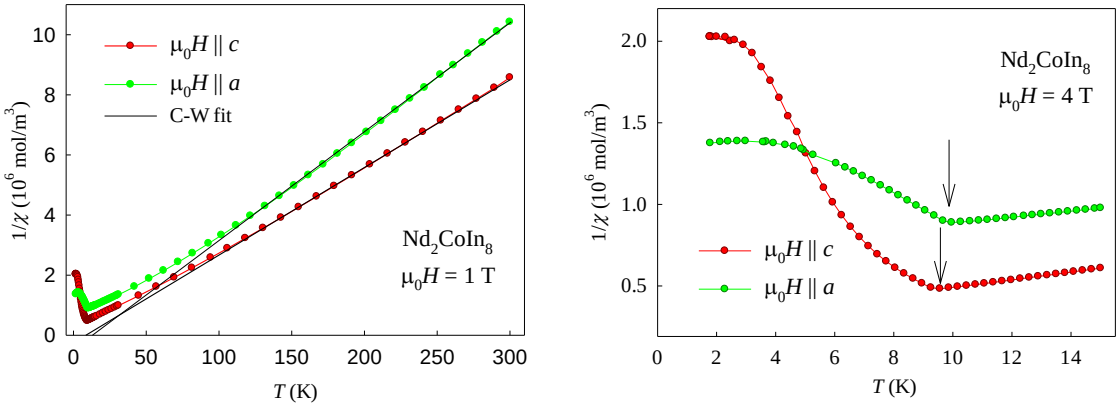

Fig. 18: The inverse magnetic susceptibility of the Nd_2CoIn_8 compound for both principal crystallographic orientations is plotted as a function of temperature on the left-hand side. The low-temperature regions of $1/\chi(T)$ are shown on the right-hand side. The arrows depict the AF transition.

The θ_P temperatures are similar for both crystallographic orientations pointing to a low anisotropy of this compound. The small and positive values of θ_P indicate relatively weak antiferromagnetic correlations and they can be partially affected also by the inaccuracy of the mass with respect to the small mass of the measured samples (~ 1 mg). A polycrystalline average of the effective moments 3.08 μ_B gives significantly lower value than expected for the free ion of Nd^{3+} (3.62 μ_B [8]) which indicates a non negligible influence of the crystal field. As expected, both the low-temperature and paramagnetic susceptibility curves of Nd_2CoIn_8 reveal lower anisotropy compared to its more 2D analog $NdCoIn_5$ [92], although the Néel temperatures of related compounds are nearly the same.

The magnetization was measured for temperatures 2 K, 8 K and 15 K (see Fig. 19). From the magnetization measurements it is evident, that the *c*-axis is the easy axis in the Nd_2CoIn_8 compound, similarly to the $NdCoIn_5$ counterpart. The preliminary results of the theoretical calculations do not agree with the magnetization

data since they prefer the *a*-axis as the easy axis in Nd_2CoIn_8 [94]. The magnetic isotherm at 2 K and 8 K shows an onset of a metamagnetic transition in the magnetic field of 6 T applied along the *c*-axis. However, higher fields would be necessary to observe the transition completely. The magnetic isotherm at 15 K measured in both directions reveals paramagnetic behaviour corresponding to the paramagnetic regime above T_N = 10 K.

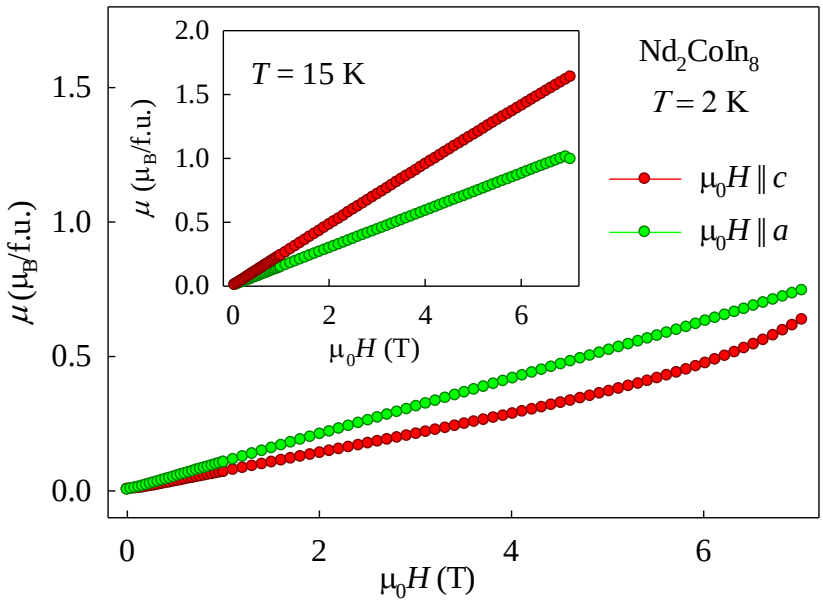

Fig. 19: Magnetic isotherm of the Nd_2CoIn_8 compound in the magnetic field oriented along *a*- and *c*-axis below (*T* = 2 K) and above (*T* = 15 K; see the inset) the transition into the AF state.

Dy_2CoIn_8

A sharp AF transition occurs around 17.5 K in zero magnetic field and another transition emerges around ~ 5 K as shown in $1/\chi$(T) data (see Fig. 20). The first transition broadens and shifts to lower temperatures in higher magnetic fields applied along the *c*-axis and the other transition disappears. Above 5 T, only one transition is distinguishable and in fields higher than 9 T there are no signs of any further magnetic transition.

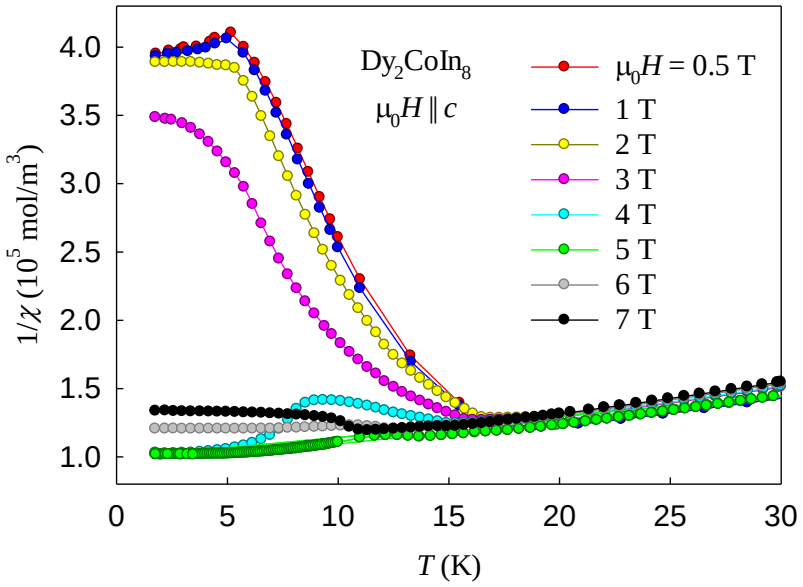

Fig. 20: Inverse susceptibility measurements of Dy_2CoIn_8 in various magnetic field oriented parallel to the *c*-axis.

The behaviour in magnetic field applied along the *a*-axis is more monotonous as the two magnetic transitions are affected by the magnetic field only weakly. The paramagnetic region of the $1/\chi$(T) data was fitted using the Curie-Weiss law (see Fig. 21) in the range 50 K - 300 K with parameters listed in Tab. 8. The small difference in θ_P

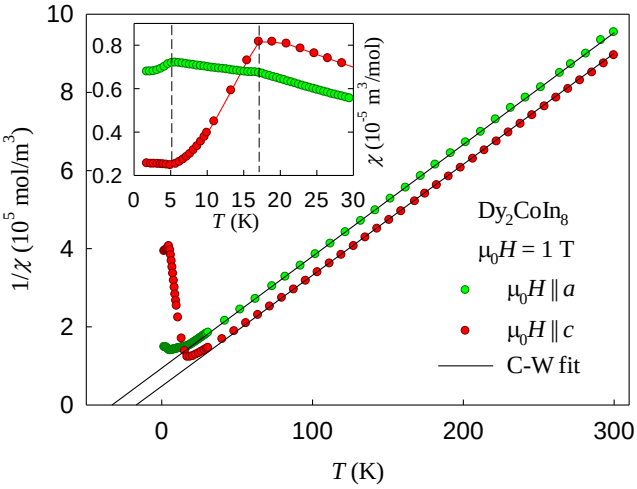

Fig. 21: Magnetization measurements of Dy_2CoIn_8 compound. The vertical dashed lines in the inset indicate the magnetic transitions.

along the *c*- and *a*-axis is a sign of a relatively small anisotropy in the PM regime and the negative values indicate AF correlations. The polycrystalline average of the effective moments along both crystallographic directions corresponds well to the value expected for the free ion of Dy^{3+} (10.63 μ_B [8]). Magnetic isotherm was measured in the temperatures 1.7 K, 2.5 K, 5 K, 8 K, 10 K and 25 K. The *c*-axis is the easy axis in the Dy_2CoIn_8 compound as shown in Fig. 22. This arrangement is also usual for other Dy_nTIn_{3n+2} compounds [80, 95] and corresponds to first principles calculations [94].

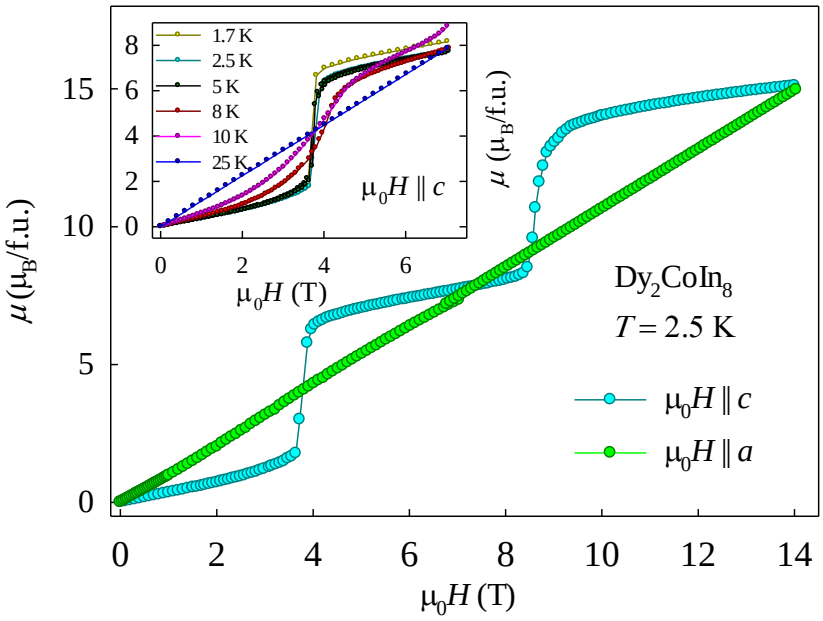

Fig. 22: The *M*(*H*) curves of Dy_2CoIn_8 at T = 2.5 K in both principal orientations of the magnetic field. *M*(*H*) curves of the Dy_2CoIn_8 in various magnetic fields oriented along the *c*-axis are shown in the inset.

The magnetic isotherm shows two metamagnetic transitions at 3.7 T and 8.6 T. The sharpness of these transitions decreases with increasing temperature. At 25 K the magnetic isotherm is a straight line indicating the paramagnetic behaviour of the material. The maximum magnetization measured at 14 T applied along the *c*-axis is 10.7 μ_B/f.u. which is slightly higher than the saturation value of the free Dy^{3+} ion (10 μ_B). This suggests that the sample can contain a negligible amount of a ferromagnetic impurity, which was not detected by other methods. The effect can also be caused by the technical reasons as the measurement was performed by the VSM apparatus.

The first metamagnetic step shown in Fig. 22 corresponds to transition to some intermediate magnetic phase in which the sum of magnetic moments equals exactly one half of the total moment in the ferromagnetic state. This can be explained by the AF ordering in one of the *ab* planes containing the Dy atom and FM ordering in the other plane. However, this arrangement does not correspond to the crystallographically equivalent positions of the Dy atoms within the structure. The second transition leads to the ferromagnetic state.

To reveal more details of the magnetic phase diagram, the specific heat was measured. Fig. 23 shows two anomalies at 5 K and 17.5 K in zero magnetic field which corresponds to the magnetic data. In higher magnetic fields the 5 K anomaly disappears gradually and the anomaly at 17.5 K shifts to lower temperature and broadens. Another transition emerges in magnetic field range from ~ 4 to ~ 6 T. No anomalies are detected in the field higher than 9 T.

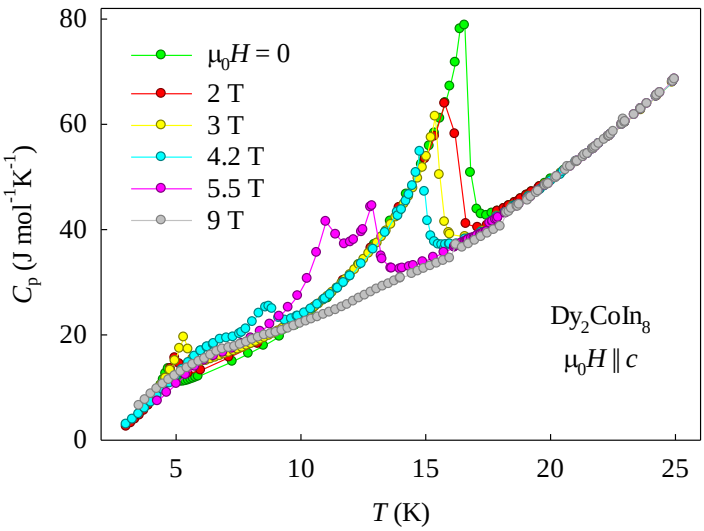

Fig. 23: Specific heat of Dy_2CoIn_8.

As the Dy_2CoIn_8 reveals a nontrivial evolution of the ground state in the magnetic field, we propose the possible magnetic field-temperature phase diagram (see the left part of Fig. 24). The low temperature region is characterized by the intermediate magnetic ordering labeled in the diagram as FM1 and increasing magnetic field induces the reorientation of magnetic moments into the FM phase labeled as FM2. Region with the antiferromagnetic order (AF) is established at higher temperatures and further increase of temperature brings the system into the paramagnetic state. The transition temperatures obtained from specific heat measurements are determined as the idealization of the specific heat jump under the

constraint of entropy conservation yields the Néel temperature. The transition temperatures obtained from magnetization temperatures are given as inflection points in the case of the $M(H)$ curves and as local maxima and minima, respectively, in the $\chi(T)$ curves.

On the other hand, the proposed phase diagram for magnetic field applied along the *a*-axis (see the right part of Fig. 24) is simpler, separated into two regions – the high-temperature region where the antiferromagnetic ordering (AF) dominates and the low-temperature region which reveals ferromagnetic order (FM). Despite the identical moment direction, the magnetic phase diagrams of Dy_2CoIn_8 and Nd_2CoIn_8 are different. The behaviour of Nd_2CoIn_8 characterized by a single antiferromagnetic phase below T_N, whereas both the specific heat and magnetization curves of Dy_2CoIn_8 reveal two additional metamagnetic transitions. These estimations of the magnetic structure need to be confirmed by further studies.

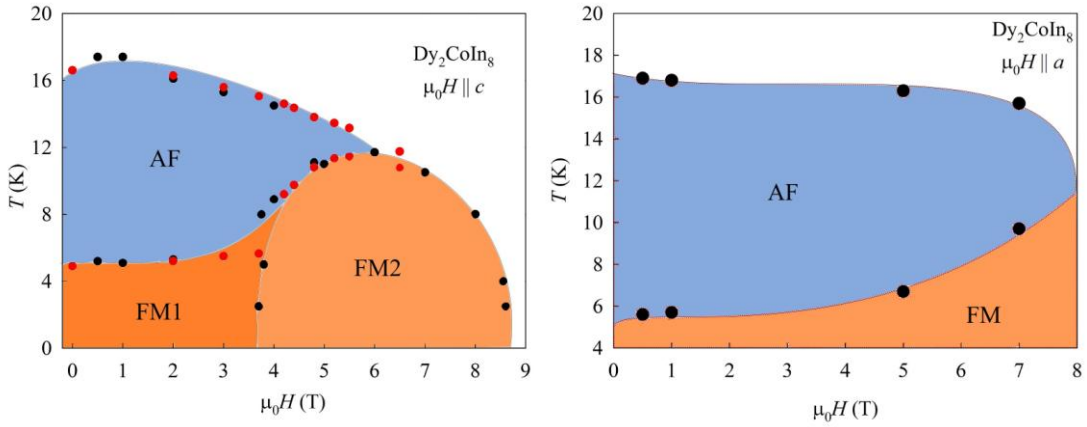

Fig. 24: Suggested temperature-magnetic field phase diagram of Dy_2CoIn_8 in the magnetic field applied along the *c*-axis (left side) and *a*-axis (right side). The red points mark values obtained from the specific heat measurements; the black points depict transition temperatures obtained from the magnetization measurements. The lines are guides for an eye with no physical meaning.

6.2. $Ce_nT_mIn_{3n+2m}$ (T = Pt, Pd)

6.2.1. Synthesis

In order to prepare single crystals of $Ce_nT_mIn_{3n+2m}$ (n = 2, 3, 5; m = 1, 2; T = Pd, Pt) phases, high purity constituent elements (Ce SSE, Pd 4N5, In 5N) in appropriate starting compositions (see Tab. 9) were used for the standard self-flux method, described in chapter 4.1. The glass tubes with the batches placed in alumina crucibles were heated up (rate ~ 200 °C/h) to the maximum temperature, kept there for several hours (8 – 10 h) to let the homogenization take place and then cooled down with a slow rate (~ 2.5 °C/h) and decanted.

High temperature attempts (1000 – 600 °C) to grow the single-phase Ce_2PdIn_8 phase were not successful because the resulted single crystals were contaminated by $CeIn_3$ which formed together with the ternary phase a "sandwich"-like structure similar to previously published data [88]. When we shifted the temperature range to lower values (750 – 550/300 °C) we have obtained a new phase Ce_3PdIn_{11} in which the grains of the Ce_2PdIn_8 phase were embedded. Further changes in the starting compositions resulted in the synthesis of the pure Ce_3PdIn_{11} phase. In contrast to Ce_3PdIn_{11}, the growth conditions for the single crystals of the $Ce_5Pd_2In_{19}$ phase have not been found yet since the Ce-Pd-In system prefers to form either the 218 or the 3-1-11 phase even from the Ce:Pd = 5:2 starting ratio.

The growth of the platinum counterparts is not as straightforward as in the previous case, although its character resembles the growth of Ce_nPdIn_{3n+2} significantly. Larger amount of other, very stable ternary phases, such as $Ce_3Pd_4In_{13}$ and $CePt_2In_7$, represents a considerable complication compared to Ce-Pd-In ternary system. The high-temperature growth led to an intergrowth of the $CeIn_3$ phase into the 218 phase similarly to the Ce_2PdIn_8 – $CeIn_3$ "sandwich" system. When the temperature range was moved to lower values (750 – 550/300 °C), a new phase Ce_3PtIn_{11} was obtained forming a "substrate" in which the grains of the Ce_2PtIn_8 phase were embedded. Again the composition change from Ce:Pt = 2:1 to 3:1 enabled to produce pure Ce_3PtIn_{11} single crystals in masses suitable for bulk measurements. However, their amount is significantly smaller than the amount of other single crystals within the batches ($CePt_2In_7$, $Ce_3Pt_4In_{13}$, $CeIn_3$). The attempts to

prepare pure single crystals of $Ce_5Pt_2In_{19}$ failed; nevertheless, single crystals of Ce_2PtIn_8 can be prepared although their typical size is only ~ 0.1 mm.

T	**Starting composition (Ce:*T*:In)**	**Temperature range (°C)**	**Final products**
Pd	2:1:25 – 40	1000 – 600	$CeIn_3$, Ce_2PdIn_8
	2:1:25 – 40	750 – 550/300	Ce_2PdIn_8, Ce_3PdIn_{11}, $Ce_5Pd_2In_{19}$, $CeIn_3$
	3:1:25 – 50	750 – 550/300	Ce_3PdIn_{11}, $CeIn_3$
	5:2:30 – 50	750 – 550/300	Ce_3PdIn_{11}, $CeIn_3$
Pt	2:1:25 – 40	750 – 550/300	Ce_2PtIn_8, Ce_3PtIn_{11}, $CeIn_3$, $Ce_3Pt_4In_{13}$, $CePt_2In_7$
	3:1:25 – 50	750 – 550/300	$CeIn_3$, $CePt_2In_7$, $Ce_3Pt_4In_{13}$, Ce_3PtIn_{11}

Tab. 9: Growth conditions of the $Ce_nT_mIn_{3n+2m}$ compounds.

6.2.2. Characterization

The $Ce_5T_2In_{19}$, Ce_2TIn_8 and Ce_3TIn_{11} phases are rather difficult to distinguish using the EDX point analysis because the difference between appropriate ratios of Ce, *T* and In is almost within the error of this approach (218 phase: 9.1:18.2:72.7; 5-2-19 phase: 7.7:19.2:73.1; 3-1-11 phase: 6.7:20:73.3). This can be clearly demonstrated on Fig. 25. The grains of the Ce_2PdIn_8 phase are embedded in Ce_3PdIn_{11} phase are shown in Fig. 25. Similar effect can be observed also in the platinum counterpart (not shown). On the other hand, these small differences can be detected using the mapping scan. As we obtained samples with multiple phases during the growth processes the EDX mapping scan of these samples became a crucial tool for detecting and distinguishing the different phases.

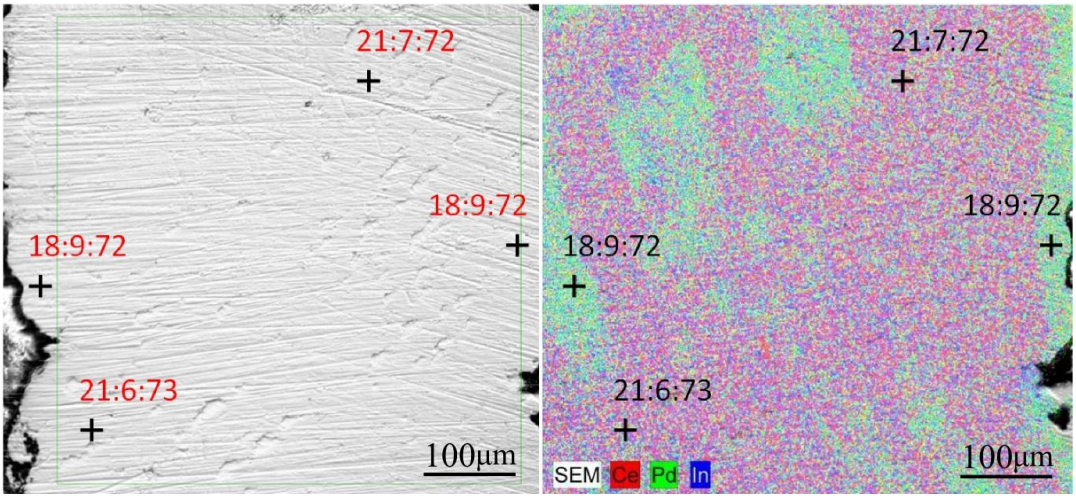

Fig. 25: BSE SEM pattern of a surface (polished to ~ ½ thickness of the Ce_2PdIn_8 single crystal) 300-times magnified. On the right-hand side, the EDX mapping of the same area is shown. The crosses depict corresponding stoichiometries obtained from EDX point analysis. One can see the clearly distinguishable grains of Ce_3PdIn_{11} phase and Ce_2PdIn_8 phase.

To obtain the structure of the phases, *X*-ray diffraction was performed on powdered single crystals. To determine the structure of Ce_3PdIn_{11}, selected single crystals from batch with the starting composition 3:1:25 were powdered. The structure of Ce_3PtIn_{11} and Ce_2PtIn_8 was determined from the synchrotron data measured on selected powdered single crystals from a batch with the initial composition 2:1:25. The *X*-ray analysis confirmed Ho_2CoGa_8 crystal structure type with the space group P4/mmm for the Ce_2PtIn_8 compound and the new structure type Ce_3PdIn_{11} [40] with the same space group was confirmed for Ce_3PdIn_{11} and Ce_3PtIn_{11} compounds. The cell parameters and atomic coordinates are listed in Tab. 10 and Tab. 11.

Ce_nTIn_{3n+2}	Cell parameters	
	***a* (Å)**	***c*(Å)**
Ce_3PdIn_{11}	4.693(2)	16.894(5)
Ce_3PtIn_{11}	4.697(3)	16.871(7)
Ce_2PtIn_8	4.699(2)	12.186(8)

Tab. 10: Lattice parameters of the studied Ce_nTIn_{3n+2} compounds.

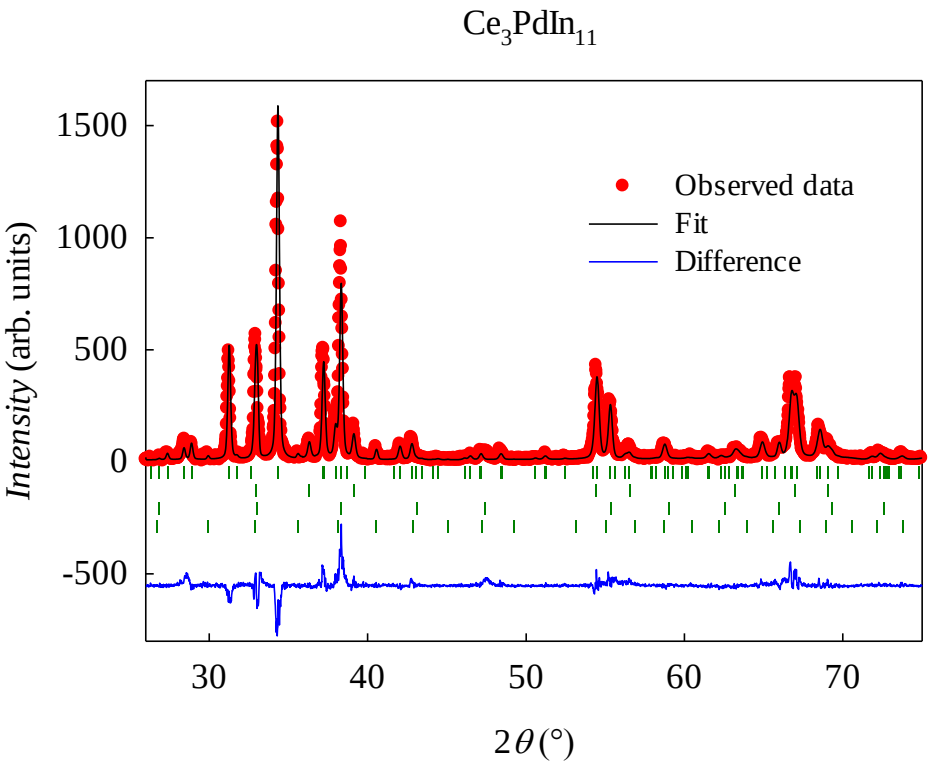

Fig. 26: Powder diffraction patterns of the powdered single crystals from the Ce_3PdIn_{11} batch. Vertical green bars show the Bragg positions of the present phases and the blue line depicts the difference between the measured data (red points) and calculated fit (black line). The phases used to fit the measured data are listed in the text.

Compound	**Wyckoff pos.**	***x***	***y***	***z***
Ce_3PdIn_{11}				
Ce1	2*g*	0	0	0.2724(5)
Ce2	1*a*	0	0	0
Pd	1*b*	0	0	0.5
In1	4*i*	0.5	0	0.4130(3)
In2	2*h*	0.5	0.5	0.2813(3)
In3	4*i*	0.5	0	0.1370(0)
In4	1*c*	0.5	0.5	0
Ce_3PtIn_{11}				
Ce1	2*g*	0	0	0.2768(9)
Ce2	1*a*	0	0	0
Pt	1*b*	0	0	0.5
In1	4*i*	0.5	0	0.4429(2)
In2	2*h*	0.5	0.5	0.2785(9)
In3	4*i*	0.5	0	0.1380(1)
In4	1*c*	0.5	0.5	0
Ce_2PtIn_8				
Ce	2*g*	0	0	0.3079(0)
Pt	1*a*	0	0	0
In1	4*i*	0	0.5	0.1221(8)
In2	2*e*	0	0.5	0.5
In3	2*h*	0.5	0.5	0.3075(7)

Tab. 11: Atomic coordinates of $Ce_nT_mIn_{3n+2m}$ compounds.

The phases used to fit all the reflections observed in the diffraction pattern from the Ce_2PtIn_8 batch are (from top to bottom) Ce_2PtIn_8, $CePt_2In_7$, Ce_3PtIn_{11}, $CeIn_3$, $Ce_3Pt_4In_{13}$ and In. The phases used for fitting the Ce_3PdIn_{11} diffraction pattern from the Ce_3PdIn_{11} batch are (Bragg positions shown in Fig. 26 from top to bottom) Ce_3PdIn_{11}, In, $CeIn_3$ and Pd_3In_7. The different phases and their weight fractions are listed in Tab. 12.

Ce:Pd:In = 3:1:25 batch	**Fract. (%)**	**Ce:Pt:In = 2:1:25 batch**	**Fract. (%)**
Ce_3PdIn_{11}	79.9	Ce_2PtIn_8	31.5
In	13.3	$CePt_2In_7$	32.7
$CeIn_3$	4.9	Ce_3PtIn_{11}	23.5
Pd_3In_7	1.9	$CeIn_3$	5.0
-	-	$Ce_3Pt_4In_{13}$	3.8
-	-	In	3.6

Tab. 12: Quantitative analysis of the diffraction patterns.

6.2.3. Physical properties

The specific heat measurements were performed on samples selected from the batches presented in Tab. 9. The samples A, B, C and D were prepared from the initial composition 2:1:25 within the temperature range 750 – 300 °C and the EDX mapping scans revealed both Ce_2PdIn_8 and Ce_3PdIn_{11} phases within the single crystals.

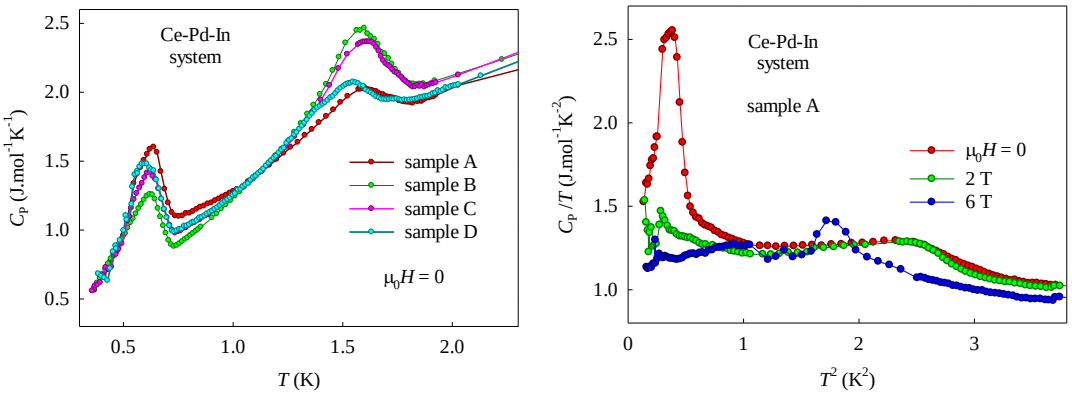

Fig. 27: Low temperature specific heat of various samples from the Ce-Pd-In system in the absence of magnetic (left). Specific heat measurements of the sample A in various magnetic fields (right).

The specific heat data reveal two transitions at T_c = 0.67 K and T_m ~ 1.7 K (see the left-hand side of the Fig. 27). Both these transitions occur in every studied sample but the ratios of the transition peaks differ from each other, which is most likely caused by different ratios of amounts of the phases in each sample. The SC transition at T_c = 0.67 K corresponds to previously observed results [63] and arises from the presence of Ce_2PdIn_8. The peak at ~ 1.7 K was observed only once before [87] and it was ascribed to a magnetic transition. Sample A was additionally measured in various magnetic fields (the right-hand side of Fig. 27). The lower transition is suppressed with increasing magnetic field which corresponds to the behaviour expected from a superconducting transition. The other transition shifts to lower temperatures with increasing field resembling an antiferromagnetic behaviour; however, in the field 6 T one can see a significant increase of the peak in the specific heat suggesting an emergence of a magnetic field-induced transition. We assume that this transition belongs to Ce_3PdIn_{11} according to the results of the EDX analysis.

As we have finally succeeded in the preparation of the single-phase single crystals of Ce_3PdIn_{11}, we have measured the specific heat of Ce_3PdIn_{11} to verify the

previous observation. The results shown in Fig. 28 confirm our assumption, as two transitions are observed at T_1 = 1.6 K and T_2 = 1.45 K. The transitions in Fig. 27 are significantly smeared out because of the higher disorder of the multiphase samples so that they look like just one, very broad transition. On the other hand, the measurement of the high quality single phase samples confirms the presence of two easily distinguishable peaks. From our measurement it is evident that the transition shown at 1.7 K [87] indicates a presence of an impurity phase – the Ce_3PdIn_{11} compound. In analogy to the results obtained from the measurement of the two-phase samples, we can assume that these peaks correspond to transitions into a magnetically ordered state. Whereas the first transition drives the compound into an AF ground state, the second transition is probably connected with a reorientation of the magnetic moments. However, this assumption has to be confirmed by further low-temperature experiments in magnetic field.

The specific heat of Ce_3PtIn_{11} single crystal is shown in the Fig. 28. Ce_3PtIn_{11} reveals similar behaviour as its counterpart with T = Pd. Two, probably magnetic transitions are observed at around T_2 = 2.0 K and T_1 = 2.1 K. The origin of these transitions has not been clarified yet and thus, further experiments in lower temperatures and higher magnetic fields are needed. However, the apparent resemblance of the behaviour of both Ce_3TIn_{11} compounds suggests similar ground state properties. The single crystals of Ce_2PtIn_8 have not been investigated by any measurement method yet due to technical difficulties caused by extremely small (< 0.1 mm) dimensions of the samples.

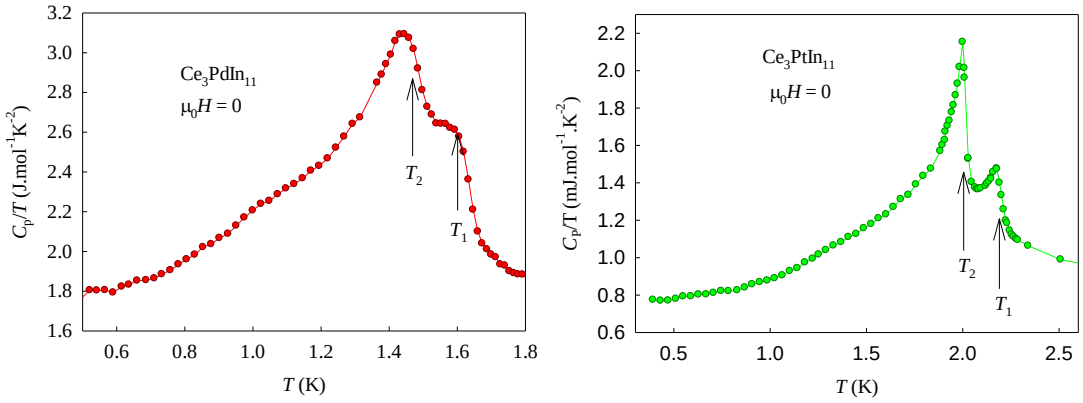

Fig. 28: The specific heat data of the Ce_3PdIn_{11} and Ce_3PtIn_{11} compounds.

A simple $C/T = \gamma + \beta T^2$ fit was utilized for Ce_3PdIn_{11} and Ce_3PtIn_{11} with results $\gamma \approx 290$ mJ.mol^{-1}Ce K^{-2} and $\gamma \approx 300$ mJ.mol^{-1}Ce K^{-2}, respectively, qualifying both

materials as HF compounds. The parameters of the fit including β and corresponding Debye temperature are listed in Tab. 13. The Debye temperatures for both compounds do not exceed 80 K, which is an exceptionably low value, indicating a need for a proper reference material to subtract the phonon part of the Debye temperature. The attempts to prepare non-magnetic analogs of the 3-1-11 compounds are forthcoming.

Ce_3TIn_{11}	**γ [mJ.mol^{-1}.K^{-2}]**	**β [mJ.mol^{-1}.K^{-4}]**	**θ_D [K]**
Ce_3PdIn_{11}	~ 290	4.9	74
Ce_3PtIn_{11}	~ 300	10.4	57

Tab. 13: Parameters of the $C/T = \gamma + \beta T^2$ fit for studied Ce_nTIn_{3n+2} compounds.

Conclusions and future plans

We have successfully prepared single crystals of the RE_2CoIn_8 (*RE* = Pr, Nd, Dy) compounds for the first time using the flux growth method. The synthesis parameters are described in detail within the results. The single crystals were carefully characterized using *X*-ray diffraction and EDX analysis and their bulk properties were studied by means of magnetization and thermodynamic measurements.

The properties of studied RE_2CoIn_8 compounds correspond to those previously studied on polycrystalline samples [50]. Moreover, the single-crystalline form of these materials enabled us to study their anisotropic properties. The *c*-axis is the easy axis for all RE_2CoIn_8 (*RE* = Pr, Nd, Dy) compounds. The calculations from first principles confirm the *c*-axis as the easy axis only in the case of Dy_2CoIn_8 [62, 94]. The large sensitivity of the crystal potential to the details of calculations is the reason that for *RE* = Pr, Nd is the easy axis different from experiment [94]. The difference between values of θ_P for both principal crystallographic orientations is relatively small for all investigated compounds. This fact points to a low anisotropy in the RE_2CoIn_8 system compared to $RECoIn_5$ system which reveals reduced 2D character. These results correspond well to the values of θ_P obtained from the analysis of $RECoIn_5$ compounds [92].

We have constructed the magnetic field-temperature phase diagram of Dy_2CoIn_8 for the field applied along the *c*-axis. As the Dy_2CoIn_8 compound resembles strongly the $M(H)$ behaviour of related Dy_2RhIn_8 [80] and undergoes two magnetic transitions in zero magnetic field, its magnetic phase diagram shows the most complex behaviour from all the known members of the non-cerium RE_nTIn_{3n+2} series [50, 69, 80, 92, 93, 95] . The diagram depicts three regions of different magnetic ordering whose character cannot be determined only by the bulk measurements. The microscopic experiments are needed to reveal the details of the magnetic moment arrangements. The presented results motivate also further experiments with single crystal synthesis of hypothetical new phases across the RE_2CoIn_8 (*RE* = Gd, Er, Tm, Yb) series.

Series of flux growth experiments with Ce-Pd/Pt-In system were performed. As a result we have successfully prepared novel phases Ce_3PdIn_{11}, Ce_3PtIn_{11} and Ce_2PtIn_8 in the single crystal form. Moreover, Ce_3PtIn_{11} and Ce_2PtIn_8 are completely new systems within the $Ce_nT_mIn_{3n+2m}$ family of compounds. The growth conditions are described in detail within the results. A careful characterization using *X*-ray diffraction and EDX analysis was performed. The bulk properties were studied by means of specific heat measurements. Our results emphasize the importance of the EDX mapping analysis as an efficient way for verification of the homogeneity of single crystals, which becomes crucial in the case of $Ce_nT_mIn_{3n+2m}$ layered structures with very close compositions.

The two-phase samples of the Ce_2PdIn_8-Ce_3PdIn_{11} system revealed both the SC transition originating from the Ce_2PdIn_8 compound and other, magnetic transition, observed in Ref. [87]. This anomaly can be ascribed to the Ce_3PdIn_{11} compound, as was confirmed by following measurements of the Ce_3PdIn_{11} single phase with two transitions T_1 = 1.6 K and T_2 = 1.45 K. The isostructural analog Ce_3PtIn_{11} shows behaviour similar to Ce_3PdIn_{11}, as two transitions can be observed at T_1 = 2.1 K and T_2 = 2.0 K. The same crystal structure of Ce_3PdIn_{11} and Ce_3PtIn_{11} corresponds well to the similar, most likely magnetic ground state properties of both heavy fermion compounds.

The Ce_nTIn_{3n+2} compounds with T = Pd are possibly the first systems were the change of the ground state from a superconducting to a magnetic one is observed, as moving towards the stronger 3D character of the structural dimensionality (Ce_2PdIn_8 - Ce_3PdIn_{11}). This possibility would enhance the importance of the dimensionality as a parameter in the extended Doniach diagram [99]. Further magnetic measurements are necessary to explain the ground state of these novel ternary systems. Our results leave open questions concerning the ground state properties of the hypothetic isostructural analogs of other transition metals, such as Ce_3RhIn_{11} or Ce_3CoIn_{11}. Last, but not least, the recent discovery of the new structure type represents certainly a motivation for synthesis of palladium and platinum 2D-counterparts such as $CePdIn_5$, $CePtIn_5$ and $CePd_2In_7$ compounds in a single crystalline form.

Bibliography

1. Stephen Blundell: Magnetism in Condensed Matter (Oxford Master Series in Condensed Matter Physics), Oxford University Press Inc., New York (2001)
2. J. Klíma, B. Velický: Kvantová teorie II, MFF UK, Praha (1990)
3. Neil W. Ashcroft, N. David Mermin: Solid State Physics, Thomson Learning (1976)
4. V. Nekvasil, M. Diviš: Localized 4*f* and 5*f* Moments: Magnetism in Encyclopedia of Materials: Science and Technology, edited by K. H. J. Buschow *et al*., p.4613, Elsevier, Oxford (2001)
5. B. Coqblin: Electron Systems: Strong Correlations in Encyclopedia of Materials: Science and Technology, edited by K. H. J. Buschow *et al.*, p.2591-2603, Elsevier, Oxford (2001)
6. J. Klíma: Kvantová teorie, lecture notes
7. P. Bruno: Introduction to Magnetism, CNR School "Physics of Spin in Materials", Chiavari, 2009, http://www.school.infm.it/documents/Bruno_1.pdf
8. C. Kittel: Introduction to Solid State Physics, 7th ed., J. Wiley & Sons, Inc. (1996)
9. N. J. Curro *et al.*, Physical review B, Volume 62, No. 10 (2000)
10. A. Lloblet *et al.*, Phys.Rev.B, Volume 69, 024403 (2004)
11. V. Sechovský: General Introduction: in Encyclopedia of Materials: Science and Technology, edited by K.H.J Buschow *et al*., p.5018, Elsevier, Oxford (2001)
12. J. Kvasnica: Termodynamika, SNTL, Praha (1965)
13. J.G. Sereni: Magnetic Systems: Specific Heat in Encyclopedia of Materials: Science and Technology, edited by K.H.J Buschow *et al.*, p.4986, Elsevier, Oxford (2001)
14. L.J. Sundström: Low temperature heat capacity of the rear earth metals, Volume 1, Chapter 5, 379-410 (1978)
15. Prasanta K. Misra: Physics of Condensed Matter, Chapter 14 – superconductivity, p. 451-468 (2012)
16. J. Bardeen, L. N. Cooper, and J. R. Schrieffer, Phys. Rev. 108, 1175 (1957)
17. H.B. Callen: Thermodynamics and an Introduction to Thermostatistics, 2nd ed., John Wiley & Sons Inc. (1985)
18. P. Monthoux *et al.*, Nature vol. 450, 1177 (2007)
19. T. Park *et al.*, Nature vol. 456, 366 (2008)

20. F. Steglich and S. Süllow: Heavy-fermion Systems in Encyclopedia of Materials: Science and Technology, edited by K.H.J. Buschow *et al.*, p.3746, Elsevier, Oxford (2001)
21. http://www.tescan.com
22. http://www.bruker.com
23. http://cmd.karlov.mff.cuni.cz/jlms/jlms
24. http://www.qdusa.com/index.html
25. Physical Property Measurement System (MPMS) – Application notes, User's Manual, San Diego
26. V. Valvoda, M. Polcarová, P. Lukáč: Základy strukturní analýzy, Karolinum, Praha (1992)
27. WinPLOTR: a Windows tool for powder diffraction patterns analysis, Materials Science Forum, Proceedings of the Seventh European Powder Diffraction Conference (EPDIC 7), 2000, p.118-123; Rodriguez-Carvajal, J., Physica B **192**, 55 (1993)
28. P. Mohn: Itinerant Electron Systems: Magnetism (Ferromagnetism) in Encyclopedia of Materials: Science and Technology, edited by K.H.J. Buschow *et al*., p.4316, Elsevier, Oxford (2001)
29. W. N. Cottingham, D. A. Greenwood: Electricity and Magnetism, ISBN: 0521368030 Cambridge University Press (1991)
30. Petr Chvosta: Termopotenciály
31. http://www.physics.oregonstate.edu/portfolioswiki/lib/exe/fetch.php?id=texts%3Athermobook%3Astart&cache=cache&media=texts:thermobook:chapter9.pdf
32. SSE II (Solid State Electrotransport): Uživatelský manuál řídícího systému, MFF UK, Praha (2001)
33. R. Abbaschian: Crystal Growth in Encyclopedia of Materials: Science and Technology, edited by K.H.J. Buschow *et al.*, p.1860, Elsevier, Oxford (2001)
34. W. Bardsley *et al.*: Crystal Growth: a Tutorial Approach 2, ISBN: 0444853715, North-Holland, New York (1979)
35. V.L. Ginzburg and L.D. Landau, *Zh. Eksp. Teor. Fiz.* **20**, 1064 (1950). English translation in: L. D. Landau, Collected papers p. 546, Oxford: Pergamon Press (1965)

36. M. Suzuki and I.S. Suzuki: Lecture Note on Solid State Physics, Ginzburg-Landau Theory for Superconductivity, Department of Physics, State University of New York at Binghamton, Binghamton, New York 13902-6000 (2007)
37. Miloš Janeček: TEM, SEM, EBSD lecture notes.
38. Fyzikální praktikum III: Optická versus elektronová mikroskopie, lecture notes
39. http://www.ill.eu/sites/fullprof/index.html
40. A. Tursina *et al.*, Journal of Solid State Chemistry 200, 7-12 (2013)
41. J.D. Verhoeven, Fundamentals of Physical Metallurgy, Wiley, New York (1975)
42. P.C. Canfield *et al., Philosophical Magazine Part B* 65, 1117 - 1123 (1992)
43. Meissner, W.; R. Ochsenfeld, *Naturwissenschaften* 21 (44): 787–788 (1933)
44. Patrick A. Lee, Phys. Rev. Lett. 71, 1887-1890 (1993)
45. K.D. Tsendin *et al.*, Journal of Optoelectronics and Advanced Materials Vol.3, No.2, p.549-552 (2001)
46. http://www.esrf.eu/UsersAndScience/Experiments/StructMaterials/ID31
47. S. Friedemann *et al.*, Nature Phys. 5, 465 (2009)
48. S. Nakatsuji *et al.*, Nature Phys. 4, 603 (2008)
49. H. v. Löhneysen: Non-Fermi Liquid Behaviour: Quantum Phase Transition In Encyclopedia of Materials: Science and Technology, edited by K.H.J. Buschow *et al*., p.6185-6191, Elsevier, Oxford (2001)
50. Devang A. Joshi *et al., J. Phys.: Condens. Matter* 19 136216 (2007)
51. H. Shishido *et al.* J. Phys. Soc. Jpn. Vol. 71 Suppl. pp. 276-278 (2002)
52. C. Pfleiderer, Rev. Mod. Phys. 81, 1551 (2009)
53. J. Paglione *et al.*, Physica C 408-410, 705-706 (2004)
54. C. Petrovic *et al.*, Europhys. Lett. 53 354 (2001)
55. E. Bauer: Kondo Systems and Heavy Fermions: Transport Phenomena in Encyclopedia of Materials: Science and Technology, edited by K.H.J Buschow *et al.*, p. 4372, Elsevier, Oxford (2001)
56. J.S. Kim *et al.*, Phys. Rev. B 69, 024402 (2004)
57. H. Hegger *et al.*, Phys. Rev. Lett. 84, 4986-4989 (2000)
58. K.H.J. Buschow *et al.*, J. Chem. Phys. 50, 137 (1969)
59. W.L. McMillan, Phys. Rev. 167, 331-344 (1968)
60. Qimiao Si, Physica B 378-380, 23-27 (2006)
61. Y.M. Kalychak, J. Alloys Compd. 291, 80 (1999)

62. M. Diviš, Physica B 407, 2524-2526 (2012)
63. K. Uhlířová *et al.*,Intermetallics 18, 2025-2029 (2010)
64. L. Hale *et al.*, J. Alloys Compd. 472, 24-29 (2009)
65. J. D. Thompson *et al.*, Journal of Magnetism and Magnetic Materials 226-230,5 (2001)
66. M.S. Brooks *et al.*, Density Functional Theory: Magnetism in Encyclopedia of Materials: Science and Technology, edited by K.H.J Buschow *et al.*, p. 2059-2070, Elsevier, Oxford (2001)
67. http://www.almath.co.uk
68. http://www.clasic.cz/index.php
69. N.V. Hieu *et al.*, J. Phys. Soc. Jpn 76, 064702-1 (2007)
70. E.G. Moshopoulou *et al.*, J. Solid State Chem. 158, 25-33 (2001)
71. Z.M. Kurenbaeva *et al.*, Intermetallics 16, 979-981 (2008)
72. D. Kaczorowski *et al.*, Phys. B (Amsterdam) 404, 2975-2977 (2009)
73. E.G. Moshopoulou *et al.*, Acta Crystallogr. B 62, 173-189 (2006)
74. R.T. Macaluso *et al.*, Chem. Mater. 15, 1394-1398 (2003)
75. J. Custers *et al.*, Nature Mat. 11, 189 (2012)
76. P.H. Tobash *et al.*, J. Phys.: Condensed Matter 24, 015601 (2012)
77. E.D. Bauer *et al.*, Phys. Rev. B 81, 180507(R) (2010)
78. D.V. Shtepa *et al.*, Vestn. Mosk. Univ. (Ser. 2), 49-197 (2008)
79. T. Park and J.D. Thompson, New J. Phys. 11, 055062 (2009)
80. P. Čermák *et al.*, Solid State Communications 163, 55-59 (2013)
81. V.I. Zaremba *et al.*, Z. Anorg. Allg. Chem. 629, 434 (2003)
82. J.K. Dong *et al.*, PHYS. REV. X 1, 011010 (2011)
83. H. Fukazawa *et al.*, Phys. Rev. B 86, 094508 (2012)
84. D. Gnida *et al.*, Phys. Rev. B 85, 060508(R) (2012)
85. N. apRoberts-Warren *et al.*, Phys. Rev. B 81, 180403(R) (2010)
86. V.H. Tran *et al.*, Phys. Rev. B 83, 064504 (2011)
87. D. Kaczorowski *et al.*, Phys. Rev. Lett. 103(2):027003 (2009)
88. K. Uhlířová *et al.*, Phys. Rev. Lett. 104(5):059701 (2010)
89. D. Kaczorowski *et al.*, Phys. Rev. Lett. 104, 059702 (2010)
90. D. Kaczorowski *et al.*, Phys. Rev. Lett. 103, 027003 (2009)
91. G. Knebel *et al.*, Phys. Rev. B 65, 024425 (2001)

92. J. Hudis *et al.*, Journal of Magnetism and Magnetic Materials 307, 301-307 (2006)
93. J.G.S. Duque *et al*., Journal of Magnetism and Magnetic Materials 323, 954-956 (2011)
94. M. Diviš – private communication
95. Y. Isikawa *et al*., Journal of Magnetism and Magnetic Materials 272-276, 635-636 (2004)
96. M. Diviš – lecture notes
97. W. Zu *et al*., Phys. Rev. B 73, 235116 (2006)
98. J.P. Perdew *et al*., Phys. Rev. Lett. 77, 3865 (1996)
99. J. Custers *et al.*, Phys. Rev. Lett. 104, 186402 (2010)